Wosnitza, E. 2002. Data analysis in thermomechanical analogue modelling. In: Schellart, W. P. and Passchier, C. W. 2002. Analogue modelling of large-scale tectonic processes. Journal of the Virtual Explorer, 7, 97-122.

Data Analysis in Thermomechanical Analogue Modelling

ELMAR M. WOSNITZA

*Geologisches Institut der Universität Freiburg,
Albertstrasse 23-B, 79104 Freiburg
email: wosnitza@uni-freiburg.de*

Abstract: Thermomechanical analogue modelling can offer new types of data, providing a way to reconstruct the stress field within the model. Recording the experiments with an infrared camera allows the thermal field of during deformation to be analysed. The materials used in thermomechanical analogue experiments were chosen to demonstrate temperature-dependent viscosities, to allow the required rheological profile due to the thermal gradient applied by the machine.

Extending known data-analysis procedures to account for irregular domains and sparse marker distributions, various strain parameters are extracted from the optical photographs, including the strain rate tensor. The viscosity distribution is obtained from the temperature field and from rheological material properties. Together with the strain-rate tensor, the viscosity allows the calculation of the stress field in the model.

Although the main purpose of this work was to set up the apparatus and to develop experimental working-procedures and data analysis, first experiments modelled simple orogenic scenarios. A modelled megathrust geometry corresponds well to seismic data from the Urals. Further models including an orogenic wedge are compared with Structures known from the Himalayas.

Keywords: Thermomechanical analogue modelling, data analysis

Introduction

Thermomechanical Analogue Modelling

In analogue models, as in numerical models, the boundary conditions and the inhomogeneities prescribed to the scenario play an important role for the outcome of the experiment. In physical models, the most significant boundary conditions under control of the experimenter are the velocities or the stresses applied to various parts of the models by controlling motors, the overall "gravity" by performing experiments in a centrifuge, and the temperature at the model boundaries by using circulators and thermostats. The inhomogeneities used in laboratory experiments include the choice of horizontally or laterally different materials, pre-formed or even lubricated thrusts and inclusions of comparatively hard or soft materials.

To simulate the rheological stratification of the earth's crust in physical models, it is necessary to take into account the variations in mechanical properties induced by variations in temperature. Until now this has been done experimentally by using materials such as sand and silicone putty, to model brittle and ductile behaviour, respectively (e. g. Davy & Cobbold, 1991). Major progress has been made in this way in understanding crustal and lithospheric processes (e. g. Chemenda et al., 1995). However, the major drawback with such models is that any material point within the model crust retains its physical properties throughout the experiment, regardless of its position within the model. Thermal readjustment is thus not taken into account, and proper scaling with respect to gravity is therefore not achieved (see Figure 1).

To investigate tectonic processes in continent-continent collision zones, in particular the role of rheology in the distribution and propagation of deformation, a deformation rig was especially designed for thermomechanical modelling. In this work, analogue materials with a temperature-sensitive viscosity were used in combination with a thermal gradient in the model to simulate the change of mechanical properties with depth.

Analogue experiments to model crustal processes using temperature dependent material properties have been made before. However, none has fully exploited all the possibilities. Oldenburg & Brune (1972, 1975) focused on structures in solidifying wax, but did not use the temperature-dependency of viscosity. Shemenda & Grocholsky (1994) examined extensional regimes using solidifying hydrocarbons and also worked on physical models of continental collision (Chemenda et al., 2000). Brune & Ellis (1997) used a temperature-sensitive viscosity of wax in an extensional set-up, Rossetti et al. (2000) modelled orogenic wedges using similar principles. None of these authors mapped the temperature distribution in the material. Nataf & Richter (1982) examined convection in fluids with temperature-dependent viscosity and mapped isolines of the thermal gradient, but no isotherms, applying their results to the evolution of planets. A historical overview of analogue modelling has been compiled by Ranalli (2001).

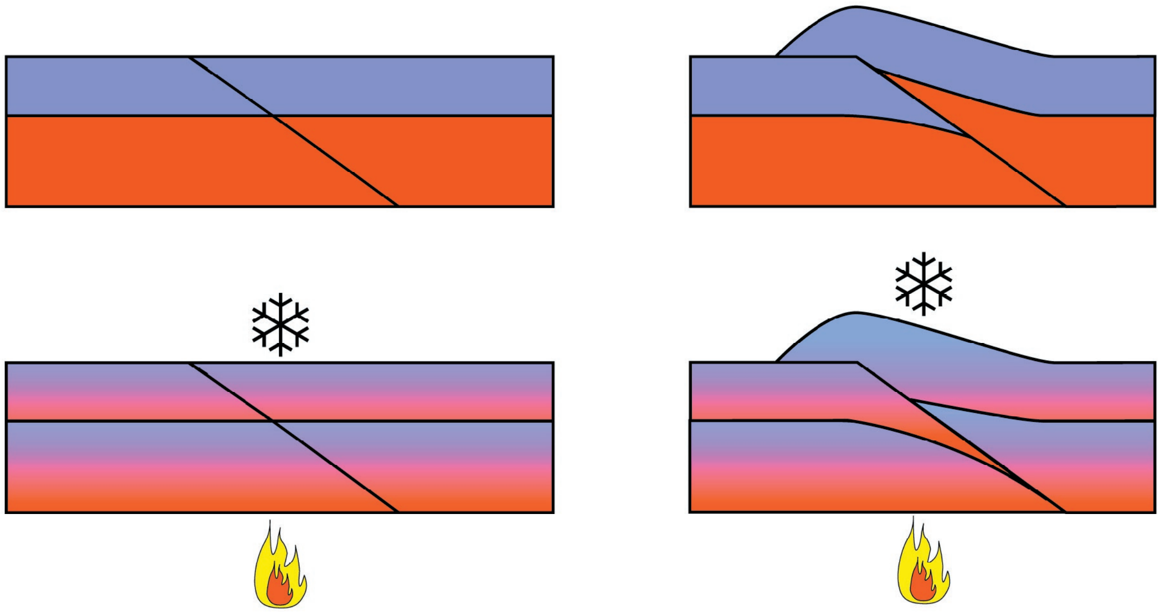

Figure 1. Concept of thermomechanical analogue modelling (bottom) vs. classical analogue modelling (top). In the classical models, material points maintain their physical properties independently of the position within the model. In thermomechanical models, temperature-dependent properties combined with a temperature gradient result in variable rheologies within one material (see tip of footwall block of upper layer).

In the experiments described by Wosnitza et al. (2001), the temperature distri-bution was mapped using an infra-red camera. The isotherms in the model could be followed through time, and their deformation was visualized. From the mechanical deformation field obtained from optical photographs, the stress field could be recovered using the known temperature-dependence of the viscosity. The combination of applying thermal boundary conditions to the model resulting in a thermal gradient and mapping the resulting temperature field throughout the deformation exploits for the first time all the possibilities of thermomechanical analogue modelling. This is a major progress in technique, since thermal readjustment in the model is not only a process used, but also documented in the experiments.

Data Analysis

Strain analysis developed for eld observations can easily be applied to analogue experiments. In the laboratory, contrary to nature, the exact geometry of the scenario is known not only at the final stage, but also before and during the deformation. Therefore, it is possible to extract more information from an analogue experiment than from analysing deformed rocks from an outcrop. However, analogue models can only offer a unique source of strain and stress data if they are properly scaled.

Mancktelow (1991) describes the analysis of a rectangular grid inscribed to the side or the top of wax models. His method requires rectangular grids, which cannot always be produced. In the experiments presented here, the blocks adjacent to the thrust are initially trapezoid. Furthermore, passive marker particles had to be added in a random distribution. These additional markers did not form a regular grid.

The algorithms developed by Bons et al. (1993) also use rectangular domains and average deformations obtained from several markers around a grid node. Therefore, this software is not applicable to relatively sparse data. The approach presented here gives results even for sparse data in arbitrarily-shaped domains.

In addition to the strain data, the temperature distribution of the experiments was used for data analysis. Such an approach has been made by Nataf & Richter (1982). Their imaging method involved the temperature-dependent refractive index of the analogue materials and mapped isolines of the temperature gradient, but not the temperature itself. As mentioned above, the thermal field can be used in combination with the deformation field to recover the stress distribution within the models.

As the load over a material point could be extracted from the above data, the lithostatic pressure at a given point can be calculated. Together with the temperature information, it was possible in this work for the first time to present pressure-temperature paths for analogue models.

Continental Collision

It is obvious, that continents can not be interpreted as rigid plates (England & Molnar, 1997). If the internal deformation of continental plates concentrates at former suture zones, the examination of processes of continental collision needs to take into account the whole lithosphere.

Building physical models with a temperature-sensitive viscosity has the advantage that the mechanical consequences of thermal readjustment during the experiment can be reproduced for lithospheric processes. This represents a major improvement in analogue models of tectonic processes. It is particularly significant for

Figure 2. Early analogue modelling done by Cadell (1889). No scaling was done for this experiment, concerned with the generation of the Scottish Highlands.

experiments investigating lithospheric stretching and the stability of mountain belts. For example, in subduction zones, the material balance is strongly controlled by the rheology of the subducted sediments (e.g. England & Holland, 1979; Mancktelow, 1995). This concept has also been applied to exhumation in collision zones (e.g. Grujic et al., 1996).

Although this work focuses on the set-up of the apparatus and the experimental procedures as well as on the data analysis, first experiments were performed to model simple orogenic scenarios. These models included the crust and the lithospheric mantle to a depth of 50 km, on a length scale of ca. 160 km. For a first set of models, the boundary of the Eastern European plate and the Kazakhstan plate at the onset of the Uralian orogenesis about 310 Ma ago (Zonenshain et al., 1994) was simplified to a single thrust. This simple megathrust geometry cutting the whole crust can be assumed for the Urals (Steer et al., 1998).

In a set of more complex experiments, the simple thrust was replaced by a wedge of weak material, as proposed for the Higher Himalayan Crystalline by Grujic et al. (1996). In these experiments, an aspect of the recent collision between India and Asia was modelled.

Scaling

For analogue models to give answers to geological questions, the models must be similar to nature in various respects. The similarity should not only be geometric, but kinematic and dynamic similarity must also be considered. This concept was first applied to geology by Hubbert (1937) who quoted Galileo Galilei:

Clearly if then one wishes to maintain in a great giant the same proportion of limb as that found in an ordinary man he must either find a harder and stronger material for making the bones, or he must admit a diminution of strength in comparison with men of medium stature; for if his height be increased inordinately he will fall and be crushed under his own weight. Whereas, if the size of a body be diminished, the strength of that body is not diminished in the same proportion; indeed the smaller the body the greater its relative strength. Thus a small dog could probably carry on his back two or three dogs of his own size; but I believe that a horse could not carry even one of his own size.

As the mass of a body and the strength of its bones scale with the cube and the square of the length, respectively, the material of the bones needs to be strengthened proportionally to the scaling of length. Accordingly, even early "analogue" experiments performed in the 19th century (see Figure 2, reproduced from Cadell 1889) used materials with properties different from those of the natural prototypes. In these attempts to explain geological processes the scaling was done rather intuitively than mathematically.

Similarities

Similarities between models and nature are rooted in processes which the model is supposed to reproduce. The physical laws governing these processes can be expressed as equations that can be used to link various properties of the model with corresponding properties in nature.

Geometric Similarity. Geometric shapes are considered to be "similar" if corresponding angles are equal. This implies that all possible ratios of lengths in the model must be the same as the corresponding ratios in nature, e. g. the aspect ratio. Exaggeration of the vertical scale does not maintain the aspect ratio. For geometric similarity all lengths must be scaled by the same scaling factor. Angles in the model must equal those in nature.

Kinematic Similarity. A prerequisite for kinematic similarity is geometric similarity. Furthermore, all the time needed for corresponding movements must be scaled by the same factor. Therefore, scaling factors for velocity, strain rate and other kinematic properties are also set by this constraint to maintain kinematic similarity.

Dynamic Similarity. Dynamic similarity deals with accelerations, forces and related properties. Therefore, the masses of corresponding volume elements dV must all be scaled by the same factor, i. e. density must be scaled homogeneously throughout the model. The relevant types of forces are:

Body Forces. Body forces act on the mass of a body. Since the density scale is given, gravitational forces $F = mg$ are only influenced by gravity g. Inertial forces can be neglected in tectonic models. Displacement rates in tectonics are of the order of some centimetres per year. To result in accelerations comparable to g, the velocities would have to be changed in the order of nanoseconds.

Surface Forces/Stresses. Forces acting on surfaces (stresses) require geometric similarity. Without this condition being fulfilled, the scaling of surface forces depends on the angle between the force and the surface normal. Stresses are to be preferred to surface forces because stresses are intensive properties.

Viscous Stresses. Instead of viscous forces, their intensive equivalent, viscous stresses should be used. These build up in a material being deformed by flowing. In order to obtain dynamic similarity with respect to viscous stresses, the viscosity must be scaled. As the viscosity of the materials in question (waxes in the model, rocks in nature) depends on temperature, the temperature dependency of the model materials must be similar to that in nature.

Thermal Similarity. In order to obtain thermal similarity, various factors have to be taken into account:

Kinematics. Kinematic similarity requires the scaling of times needed for corresponding mechanical movements. Consequently, thermal relaxation times must also be scaled. Thus, advective heat transfer (governed by mechanical movement) and conductive heat transfer (governed by thermal diffusion) are treated equally.

Rheology. To obtain dynamic similarity with respect to viscous stresses, the temperature-dependent rheology in the model needs to follow the same type of relationship as in nature. This leads to a scaling factor for the activation energy.

Energy. In general, temperature-related properties referring to thermal energy such as thermal conductivity or heat flux must be scaled as well. Nevertheless, if thermal energies do not contribute to the deformation, this demand can be neglected.

The concept of similarities leads to three different approaches which are mathematically equivalent:

1. Dimensionless Numbers

One way to verify similarities is to use dimensionless numbers, i. e. ratios of properties sharing the same dimension within one system. Equality of the dimensionless numbers then ensures similarity between model and nature. Using dimensionless numbers, several systems can easily be compared quantitatively (Ramberg, 1967; Ranalli, 1987).

2. Non-Dimensionalisation

Instead of using ratios of properties sharing the same dimension, the concept of non-dimensionalisation uses characteristic values of any property to obtain dimensionless values (Weijermars & Schmeling, 1986). This extension of the concept of dimensionless numbers requires several equations linking the characteristic values to be fulfilled.

3. Scaling Factors

In this work, ratios between corresponding values in the model and in nature ("scaling factors") are used. Some of these scaling factors can be chosen arbitrarily, others are set by equations linking the scaling factors. This concept offers large flexibility, and inconsistencies in the scaling are easily visualized (Hubbert, 1937; Ramberg, 1967). The next section describes the scaling factors as well as the equations linking them.

Parameters Scaled

Time, Velocity and Length

In these experiments advantage was taken of the differences in rheology induced by the thermal gradient within the material. One of the main demands on scaling was therefore that thermal velocities were scaled by the same factor as mechanical velocities.

The equation governing heat transfer in thermally isotropic materials, without internal heat production, is

$$\frac{\mathrm{d}T}{\mathrm{d}t} = \frac{\partial\left(\kappa\frac{\partial T}{\partial x_i}\right)}{\partial x_i}. \tag{2.1}$$

During deformation, thermal and mechanical velocities must be treated equally. Thus, it must be ensured that the time needed by material particles or heat to move over a certain distance is scaled by the same factor. For the scaling factors of length l, time t and thermal diffusivity κ,

$$S_t = \frac{{S_l}^2}{S_\kappa} \tag{2.2}$$

can be obtained, where the scaling factors S_X of a property X represent the ratio of laboratory values to natural values. Equation 2.2 couples the length and time scales to the material-dependent scale of thermal diffusivity.

The length and time scales are also coupled by the request for kinematic similarity. All velocities in the model must be scaled by the same factor

$$S_v = \frac{S_l}{S_t}. \tag{2.3}$$

The thermal diffusivity of rocks is about $10^{-6}m^2s^{-1}$ (e.g. Ranalli, 1987; Fowler, 1990, ch. 7), whereas that of paraffin wax is about $8x10^{-8}m^2s^{-1}$ (Rossetti et al., 1999). This results in a scaling factor $S\kappa$ of $8x10^{-2}$. Orogenic convergence rates are in the range 1-5cm/a (e.g. Pfiffner & Ramsay, 1982). The experimental convergence velocities 8-10μm/s chosen for the experiments are therefore scaled by $2.5x10^4$. From the resulting scaling factor for time of $1.26x10^{-10}$, and using equation 2.3, the scaling factor for length is found to be $3.17x10^{-6}$. As a consequence, the initial model length of 45cm corresponds to a length in nature of about 140km, and one hour of experiment time corresponds to a geological time of 0.9Ma.

The scaling of length is limited by the size of the smallest particles used in the experiments. The grains of the brittle material used are smaller than 200μm, which scale to 63m in nature. The process of the data analysis uses markers with a spacing of the order of centimetres, limiting the interpretation of the experiments to lengths larger than 3 km.

Viscosity and Stress

In the model, as in nature, gravity g acts on a material unit with a density ρ and a thickness h, resulting in gravitational stresses σ_{grav}. Gravitational stresses need to have the same scaling factor as viscous stresses σ_{visc}, where the latter result from deforming a material with a linear viscosity η at a strain rate ε. Because of:

$$\sigma_{\mathrm{visc}} = \eta\dot{\varepsilon} \tag{2.4}$$

and

$$\sigma_{\mathrm{grav}} = \varrho g h \tag{2.5}$$

the model is only scaled to gravity when

$$S_\eta = S_\varrho S_g S_l S_t. \tag{2.6}$$

This also implies the scaling factor for stresses to be

$$S_\sigma = S_\varrho S_g S_l. \tag{2.7}$$

In experiments, where the length and time scales are only coupled by limitations for the scaling of velocity, equation 2.6 can be used to vary the scaling factor for time. In these cases, a centrifuge is needed to vary S_g (e. g. Koyi & Skelton, 2001; Koyi, 2001).

The mean densities of the upper and lower crust are 2800 kg/m^3 and 3300 kg/m^3, respectively (Fowler, 1990). The densities of the according analogue materials Jet-Plast and paraffin wax are 736 kg/m^3 and 882 kg/m^3. The resulting scaling factor for density $S\rho = 0.26$ applies for both upper and lower crust. Using equation 2.6 and 2.7, scaling factors for viscosity and stress are found to be $S\eta=10^{-16}$ and $S\sigma=8x10^{-7}$.

The scaling factor for viscosity can be used to determine the viscosities needed in the analogue model. For this, the viscosities of natural rocks must be calculated from published flow parameters and an assumed geothermal gradient. Using a geotherm of 20°C/km typical for a

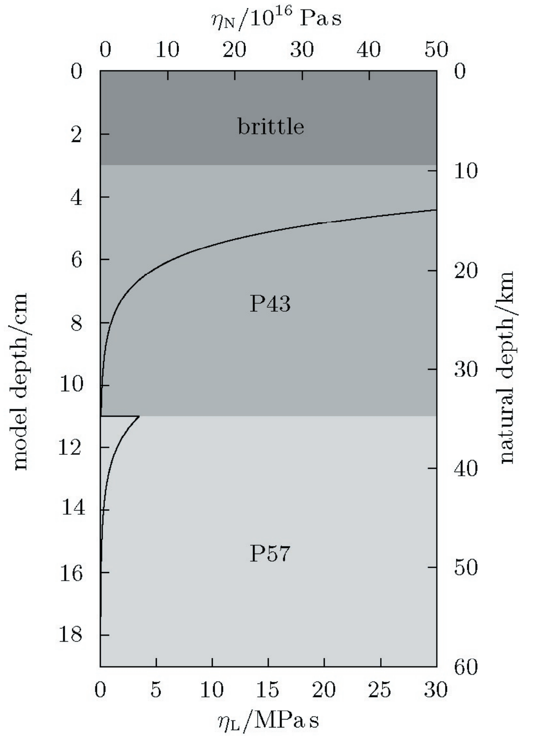

Figure 3. Rheological stratification in the experiment. In the top layer, the Jet-Plast shows Mohr-Coulomb rheology. The viscosities of the two wax layers are determined using the parameters presented in Table 7. The viscosity contrast at the depth of 11 cm is about 4MPa. Note that the horizontal scale gives viscosities instead of fracture strengths. The latter are commonly found in the literature (e. g. Ord & Hobbs, 1989; Handy et al., 2001; Kirby & Kronenberg, 1987; Carter & Tsenn, 1987), but are inappropriate for viscous (Newtonian) materials.

convergent collisional orogenic setting (e. g. Decker et al., 1988), a wide range of viscosities can be found. Basing on parameters from Carter & Tsenn (1987) for “wet” dunite and a temperature of 720°C at a depth of 35km, a viscosity of $3.1x10^{22}$ Pa s is obtained for the top of the upper mantle. Scaling this value to the laboratory using $S\eta = 10^{-16}$, the viscosity for the wax needs to be 3.5MPas. This viscosity can be reached using the paraffin wax P57 at a temperature of 42.3°C, which is close to the melting point of the other paraffin wax (P43). In order to have the base of the upper mantle as weak as the base of the lower crust, a temperature of around 56°C must be set at the model base. Since the above depth of the Moho scales to 11 cm in the model and an overall lithospheric thickness of 60km scales to a model height of 19 cm, the required thermal gradient in the experiments turns out to be 1.7°C/cm. These arguments leads to the viscosity profile for the model shown in Figure 3.

According to Weijermars & Schmeling (1986), rheological similarity also demands equality of the dimensionless stress exponents for natural and analogue materials. This exponent is between 1.8 and 5.1 for the materials shown in Table 2. For the paraffin waxes used, the measured data is consistent with $n = 1$. Rossetti et al. (1999) obtained similar low ($n < 1.3$) stress exponents, while Mancktelow (1988) gave values between 2.4 and 4.1. This value is only significant in scenarios with large gradients in the strain rate.

Property	Equation		Scaling	
Heat flux	$\vec{I} = \lambda \vec{\nabla} T$	$\Leftrightarrow$	$S_I = \frac{S_\lambda S_T}{S_l}$	(4.1)
Th. expansion	$\frac{\mathrm{d}V}{V} = \alpha\,\mathrm{d}T$	$\Leftrightarrow$	$S_\alpha = {S_T}^{-1}$	(4.2)
Mass	$m = \varrho V$	$\Leftrightarrow$	$S_m = S_\varrho {S_l}^3$	(4.3)
Strain rate	$\dot{\varepsilon} = \frac{\frac{\mathrm{d}l}{l}}{\mathrm{d}t}$	$\Leftrightarrow$	$S_{\dot{\varepsilon}} = {S_t}^{-1}$	(4.4)
Time	$m\frac{\mathrm{d}^2x}{\mathrm{d}t^2} = kx$	$\Leftrightarrow$	$S_t = \sqrt{\frac{{S_l}^3 S_\varrho}{S_k}}$	(4.5)
Acceleration	$g = \frac{\mathrm{d}^2h}{\mathrm{d}t^2}$	$\Leftrightarrow$	$S_g = \frac{S_v}{S_t}$	(4.6)

Table 1. Additional equations for scaling of thermomechanical analogue experiments. These equations are not considered in the experiments presented here. The effects involved are negligible (4.6, 4.5), do not contribute to the deformation (4.1), or they are trivial (4.3, 4.4).

S_η in the lower crust				S_η in the upper mantle			
Material	Ref.	top	mid	Material	Ref.	top	mid
Quartzite	(1)	5.8×10^{-15}	2.6×10^{-15}	dry Dunite	(1)	2.9×10^{-17}	4.3×10^{-17}
Quartzite	(1)	4.2×10^{-16}	2.0×10^{-14}	wet Dunite	(1)	$\mathbf{1.0\times10^{-16}}$	5.9×10^{-17}
Qz.-Diorite	(1)	2.8×10^{-17}	1.1×10^{-15}	wet Dunite	(1)	2.3×10^{-16}	5.7×10^{-17}
Marble	(1)	3.3×10^{-15}	1.0×10^{-15}	Dunite	(3)	3.8×10^{-16}	3.6×10^{-16}
Granite	(1)	1.5×10^{-16}	3.9×10^{-16}	Olivine	(3)	2.1×10^{-17}	3.3×10^{-17}
Granite	(1)	2.0×10^{-15}	2.2×10^{-14}	Olivine	(3)	3.1×10^{-17}	5.1×10^{-17}
Diabase	(1)	7.3×10^{-18}	1.3×10^{-16}				
dry Quartzite	(2)	5.2×10^{-17}	3.0×10^{-16}	(1) Carter & Tsenn (1987)			
wet Quartzite	(2)	1.2×10^{-15}	3.2×10^{-14}	(2) Ord & Hobbs (1989)			
Anorthosite	(2)	9.1×10^{-18}	1.1×10^{-16}	(3) Kirby & Kronenberg (1987)			

Table 2. Scaling of viscosity. Depending on the parameters for the materials chosen, different rheological scenarios are possible. In this table, the scaling factor for viscosity S• is given for various earth materials in different depths (top and middle of lower crust and upper mantle). The values were calculated from properties given in the references. The scaling factor of 1.0x10-16 as calculated from the scaling factors for length, time and density is reached for wet dunite at the depth of the top of the upper mantle. Furthermore, the model turns out to be scaled for a lower crust composed of granites, which is plausible.).

Temperature

To check the scaling factor for the absolute temperature T, consider the temperature-dependent flow law for polycrystalline aggregates. This relation is often expressed in power-law form as

$$\frac{\dot{\varepsilon}}{\dot{\varepsilon}_0} = \left(\frac{\sigma}{\sigma_0}\right)^n e^{-(H/RT)} \qquad (2.8)$$

or more commonly as

$$\dot{\varepsilon} = A\sigma^n e^{-(H/RT)} \qquad (2.9)$$

where

$$A = \dot{\varepsilon}_0 {\sigma_0}^{-n} \qquad (2.10)$$

(Means, 1990).

This equation does not influence the scaling factors for stress or strain rate, but it requires the exponent

$$\frac{H}{RT} \qquad (2.11)$$

to be dimensionless. Because of $S_R = 1$,

$$S_H = S_T. \qquad (2.12)$$

The activation energy for the paraffin waxes used was measured to be about 420 kJ/mol (see Table 7). For the dunite mentioned above, around 500 kJ/mol were given by Carter & Tsenn (1987). This results in a scaling factor for the activation energy of 0.84. The ratio of the absolute temperatures at the "Moho" (315 K in the model, 1000 K in nature) is 0.3. Therefore, temperature is not correctly scaled. Since the activation energy influences the curvature of the profile shown in Figure 3, correct scaling of the temperature should cause the profile to bend more sharply. Consequently, the scaling of the viscosity is correct at the depth of the Moho only. Table 2 gives the actual scaling factors for viscosity for different depths and different parameters, resulting in values for $S\eta$ between $7\text{x}10^{-18}$ and $3\text{x}10^{-14}$. The variation at a constant depth of up to three orders of magnitude is due to variations in the measured parameters for lithospheric rocks. Furthermore, the data for natural rocks is gained from samples which are small compared to the areas modelled, which contributes to the uncertainties (Handy et al., 2001).

Using materials with lower activation energies such as colophony (Cobbold & Jackson, 1992, H = 255 kJ/mol) would improve the quality of scaling. Materials with a larger activation energy such as the paraffin used by Rossetti et al. (1999) result in a required scaling factor for temperature larger than one. In that case, the temperatures in the laboratory should be larger than those in nature, in order to provide correct scaling.

Input	$\kappa_{\mathrm{L}}, \kappa_{\mathrm{N}}$	$v_{\mathrm{L}}, v_{\mathrm{N}}$		l_{L}	$\varrho_{\mathrm{N}}, \varrho_{\mathrm{L}}$		T_{N}	Eqn. 2.15		T_{N}
	$\downarrow$	$\downarrow$		$\downarrow$	$\downarrow$		$\downarrow$	$\downarrow$		$\downarrow$
Output	S_κ	S_v	$\rightarrow S_l, S_t$	$\rightarrow l_{\mathrm{N}}$	S_ϱ	$\rightarrow S_\sigma, S_\eta$	$\rightarrow \eta_{\mathrm{N}}$	$\rightarrow \eta_{\mathrm{L}}$	$\rightarrow T_{\mathrm{L}}$	$\rightarrow S_T$

Table 3. Scaling thermomechanical experiments. Given or desired parameters are shown in the top row. From these, various scale factors and properties can be calculated (bottom row) and checked against each other (see text).

Quantity		Nature	Laboratory	Scale
Thermal diffusivity	κ	$10^{-6}\,\mathrm{m^2s^{-1}}$	$8\times10^{-8}\,\mathrm{m^2s^{-1}}$	8×10^{-2}
Velocity	v	$1\,\mathrm{cm\,a^{-1}}$	$8\,\mathrm{\mu m\,s^{-1}}$	2.5×10^{4}
Length	l	160 km	50 cm	3.2×10^{-6}
Time	t	0.9 Ma	3600 s	1.3×10^{-10}
Density	ϱ	$3300\,\mathrm{kg\,m^{-3}}$	$880\,\mathrm{kg\,m^{-3}}$	0.26
Stress	σ	1.7 GPa	1.5 kPa	8.5×10^{-7}
Viscosity	η	$3.1\times10^{22}\,\mathrm{Pa\,s}$	$3.5\times10^{6}\,\mathrm{Pa\,s}$	1.1×10^{-16}
Activation energy	H	500 kJ/mol	420 kJ/mol	0.84
Temperature	T	720 °C	42 °C	
		1000 K	315 K	0.3
Internal friction	φ	35°	37°	1.05

Table 4. Scaling factors for the experiments described. The numbers are calculated according to Table 3. Density is given for the ductile materials. For the brittle materials, density is scaled by the same factor. The stresses given are lithostatic stresses at the model base and at the corresponding depth in nature. The value for viscosity was calculated for the top of the upper mantle using parameters for a wet dunite given by Carter & Tsenn (1987). Effective scaling factors for viscosity can differ by some orders of magnitude, depending on material parameters and chosen depth, as is shown in Table 2.

However, following an argument of Cobbold & Jackson (1992, p. 257), only the first two or three orders of magnitude of the overall strength variation are likely to have significant mechanical consequences. Whether the weaker layers are weaker by four or by five or even more orders of magnitude does not influence the stiffness of the overall scenario. Therefore, an attempt to perfectly scale the experiments for temperature is probably unnecessarily rigorous.

Nevertheless, "pseudo-temperatures" may be given for the model. These temperatures can be used in *PTt* paths (see sections 3.3.3 and 4.2.5). To scale a model temperature T_L to nature, the following "work-around" for the scaling of temperature is proposed:

$$\begin{tikzcd} z_{\mathrm{L}} \arrow[r, "S_l"] & z_{\mathrm{N}} \arrow[d, "T_{\mathrm{N}}(z_{\mathrm{N}})"] \\ T_{\mathrm{L}} \arrow[u, "T_{\mathrm{L}}(z_{\mathrm{L}})"] \arrow[r, "\cancel{S_T}"] & T_{\mathrm{N}} \end{tikzcd}$$

Here, the thermal gradient in the laboratory $T_L(z_L)$ is used to calculate a corresponding "depth" z_L . Using the scaling factor for length S_L, z_L is converted to a natural "depth" z_N. From the latter, the natural temperature can be reconstructed using $T_N(z_N)$. "Depth" in this context is not to be taken literally since it describes the depth in a scenario with a homogeneous geothermal gradient. Instead of a simple scaling factor, the proposed work-around provides the linear relationship

$$T_{\mathrm{N}}/\ \mathrm{C} = 37 \times T_{\mathrm{L}}/\ \mathrm{C} - 840. \tag{2.13}$$

This approach has certain drawbacks:

- Phase transitions in either material are ignored, although they are essential in the reconstruction of natural *PTt* paths. Phase transitions also influence the overall rheology of crustal and mantle materials.
- In some cases, unrealistically low temperatures are obtained for the upper crust. This is due to the thermal conductivity of the brittle material which is different from the conductivity of the waxes.
- The incorrect scaling of temperature does not only obstruct the direct way from T_N to T_L. It also causes the flow laws in the laboratory and in nature to be not exactly similar. Thus, only in the stronger parts of the materials does that relationship hold.

Therefore, the temperatures obtained this way should be used with caution. Nevertheless, at the present stage of this work, this is the only way to gain temperature predictions from the analogue experiments.

Brittle Behaviour

The rheological behaviour of brittle rocks can be described by using the angle of internal friction and the cohesion σ_c to determine the fracture strength σ_f from the lithostatic pressure σ_{lith}

$$\sigma_{\mathrm{f}} = \sigma_{\mathrm{c}} + \sigma_{\mathrm{lith.}} \tan\varphi, \tag{2.14}$$

neglecting pore pressure effects (Hubbert & Rubey, 1959).

The angle of internal friction is dimensionless, therefore it must be equal in the model and in nature. Jet-Plast, the brittle material chosen has an angle of internal friction of (37±2)°. Natural brittle rocks show angles of internal friction of 25°-35° (e. g. Lallemand et al., 1994). Although the scaling in this case is not perfect, the error bars overlap.

Cohesion is a stress, consequently it needs to be scaled with the scaling factor for stresses. According to Hoshino et al. (1972), crustal rocks show cohesions of <20 MPa. In fact, these values were measured for rather small samples (some centimetres height). Due to pre-existing fractures, the bulk cohesion of the upper crust might be lower. Sand has cohesions of 20 -170 Pa (Lallemand et al., 1994). Due to the composition of the Jet-Plast, electrostatic forces can be assumed to lead to a lower cohesion. The upper limit of the natural cohesions scales down to 17 Pa which is well in the plausible range for the model material.

Consistency of Scaling

When scaling analogue experiments, priorities have to be set, because scaling of all possible properties is not possible. In the experiments presented here, there are four free parameters:

- convergence rate,
- surface temperature,
- base temperature and
- initial length.

The initial height of the model (thickness of the lithosphere) does not influence the scaling and is therefore omitted here.

Once a material or a set of materials has been chosen, four material properties are important:

- thermal diffusivity,
- density,
- viscosity and
- activation energy.

Equations 2.2, 2.3, 2.6 and 2.12 couple the eight scales for length, time, viscosity, density, gravity, thermal diffusivity, activation energy and temperature. Furthermore, the Arrhenius Equation

$$\eta(T) = \eta_0 e^{\frac{H}{R}\left(\frac{1}{T}-\frac{1}{T_0}\right)}, \tag{2.15}$$

where η_0 is the viscosity at a chosen temperature T_0, couples the material properties viscosity and activation energy.

In the experiments presented here, the scaling factors were determined by following the steps given in Table 3. A summary of the resulting scaling factors for the properties discussed above can be found in Table 4. Having chosen a material, the thermal diffusivity is given and the corresponding scaling factor is fixed. The limitations of the deformation apparatus set the velocity scale. From these two, the length and time scales were calculated. After that, limits for length of the natural scenarios to be modelled could be estimated from the possible initial lengths in the laboratory.

Since the density scale was set by the choice of materials, the scales for stress and viscosity were also given. From the viscosities in nature, those to be used in the laboratory can be calculated, thus determining the temperatures to be used in the experiments.

On the other hand, equation 2.12 couples the temperature scale to the scale for the activation energy, a material property. This relationship overdetermines the problem by adding a further restriction. In the case of the experiments presented here, the absolute value of temperature is the only property being scaled inconsistent with the other properties: The scaling of temperature is off by a factor of two.

Parameters Not Scaled

In analogue models, not all parameters can be scaled. In contrast to the properties consistently scaled, other parameters were not considered in the experiments described in this work. Of some, it can be safely assumed that they do not influence the system on the time-scale or length-scale modelled, such as solar radiation: diurnal surface temperature variations fall to 1% at 1.5m depth, annual variations at 25 m, both lengths being below the resolution for the scaling of length.

Further thermal parameters such as conductivity or heat flux (equation 4.1) concern thermal energies. Since the experiments were performed at temperatures above the phase transition temperature of paraffin waxes of around 26°C (Mancktelow, 1988), effects of thermal energies can be neglected. In addition to these thermal properties, other relationships such as those given in Table 1 can be found, overdetermining the problem even further. Some of these equations are trivial (e. g. equations 4.3 or 4.4). Others describe relationships which are irrelevant to the modelled scenario. For example, elastic properties described by equation 4.5 can be neglected due to the low strain rates.

Other parameters do influence the system, but cannot be scaled; in fact they cannot be modelled. Sedimentation (e. g. Cobbold et al., 1989; Vendeville & Cobbold, 1988; Sans & Koyi, 2001) and erosion (e. g. Davy & Cobbold, 1991) have been used in analogue modelling. These experiments were done episodically: the deformation was stopped to perform the sedimentation. In the models presented here, the scaling of time prohibited to stop the experiments for sedimentation or erosion: the heat flux could not be stopped. Furthermore, the thermal insulation around the model would have to be disturbed strongly. Nevertheless, numerical models suggest that erosion and sedimentation significantly influence the deformation and its localisation during orogenesis (e. g. Willett et al., 1993; Jamieson et al., 1996).

Data Analysis

Experimental Data

Raw Data

To examine the strain distribution in the model, the deformation field has to be analysed. The movement of passive markers can provide the necessary information.

These markers can either be small particles or a passive grid inscribed into the wax. The markers need to act passively during the deformation of the model, i. e. they must neither give additional strength nor show movement of their own (e. g. gravitationally). Furthermore, the markers should provide a good optical contrast with the surrounding material to be visible and identifiable on photographs.

In the experiments presented here, a passive grid was used to visualize the bulk deformation during the experimental phase. Because of melting in the lowermost part of the experiment, parts of this grid lost contrast during deformation. Therefore, small (≈1 mm) coloured plastic particles were added to increase the number of markers. Nevertheless, markers that left the visible domain (in wax melting at the model base or moving behind the pistons) could not be used. The total number of markers (particles and grid points) in each experiment was between 160 and 640.

Optical images were taken during the deformation using a black and white digital camera. These images show the side view of the analogue models. After each experiment, it was verified that the deformation was homogeneous in the line of view, i. e. that the images represented the deformation within the model.

Simultaneously with the optical images, infra-red images were recorded. They offer a theoretical resolution of 0.3 K, but due to the necessary calibration described by Wosnitza et al. (2001) the error is about 2 K.

Data Preparation

Before data analysis, the optical images had to be processed. All the markers visible on each of the successive photos were selected and were assigned a number, using an image processing software (Adobe Photoshop). Subsequently, the positions of the markers were digitized on the computer screen using routines of plot_grid (Mancktelow, 1991). The markers of each block of material were digitized separately to allow for movement along the block interfaces.

From the coordinates of the markers within each block of material, a Delaunay Triangulation (the smallest occurring angle is as large as possible, Wolfram 1991) was calculated, and triangles with lines outside the block were removed using a routine from Sedgewick (1988). The triangulation of the initial stage of the experiment provided the connectivity list for all other subsequent time steps. This topology was followed through time, and the change of its geometry was analysed.

In this analysis, the overall strain can be considered as being homogeneous within one triangle. All subsequent considerations refer to the deformation of the single triangles.

The experiments show no significant inhomogeneities in the third dimension, perpendicular to the transport direction. Therefore, the deformation in this direction can be neglected, and a two-dimensional approach is sufficient.

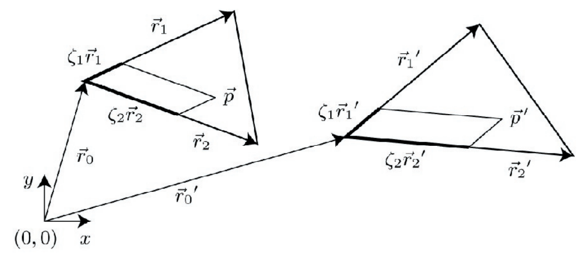

Figure 4. Triangle before and after deformation From the transformations r1• r1’ and r2• r2’, various strain properties can be calculated. The coordinates of a point p within a triangle can be expressed in terms of the sides of that triangle. Those pseudo-coordinates •1 and •2 do not change, as long as deformation is homogeneous in the domain in question.

Strain Analysis

In an area of homogeneous strain, the deformation can be described as linear coordinate transformation. In general, this transformation can be split into translation, rotation and deformation.

Strain Matrix

Disregarding translation, the Lagrangian formulation of the coordinate transformation equations in two dimensions is

$$\begin{aligned} x' &= ax + by \\ y' &= cx + dy, \end{aligned} \tag{3.1}$$

which leads to the strain matrix ε defined by

$$\vec{r}\,' = \hat{\varepsilon}\vec{r} \tag{3.2}$$

(Ramsay & Huber, 1983), where

$$\hat{\varepsilon} = \begin{pmatrix} a & b \\ c & d \end{pmatrix}. \tag{3.3}$$

The relative movement of the three vertices of a triangle can be used to determine the strain matrix for that triangle. For this, the coordinates of two vertices are expressed relative to the third, which is taken as the origin. Thus, movement of the whole triangle does not contribute to the internal deformation. For a triangle defined by r_0, $r_0 + r_1$ and $r_0 + r_2$ (see Figure 4) the deformation matrix ε can be found solving

$$\begin{aligned} \vec{r}_1{}' &= \hat{\varepsilon}\cdot\vec{r}_1 \quad \text{and} \\ \vec{r}_2{}' &= \hat{\varepsilon}\cdot\vec{r}_2 \end{aligned} \tag{3.4}$$

simultaneously. This is possible as long as r_i are not parallel, i. e. the triangles enclose non-zero area.

Strain Ellipse
The angle between the coordinate axes and the principal strains can be found from the entries of the strain matrix using

$$\tan\vartheta = \frac{2(ac+bd)}{a^2+b^2-c^2-d^2} \tag{3.5}$$

(Ramsay & Huber, 1983). A useful way to visualize strain is the strain ellipse (Ding, 1984). It shows the deformation of a circle inscribed on the object in question. Knowing the strain matrix ε, the properties of the strain ellipse can be calculated. The equation defining the strain ellipse is

$$\left(\frac{dx'-by'}{ad-bc}\right)^2 + \left(\frac{-cx'+ay'}{ad-bc}\right)^2 = 1 \tag{3.6}$$

(Ramsay & Huber, 1983). By rotating (x',y') in equation 3.6 back to (x, y) using a rotation matrix around ϑ from equation 3.5, the principal strain axes and the coordinate axes coincide. The principal strains e_x and e_y can now be obtained from the coefficients $(1 + e_x)$ and $(1 + e_y)$ of x^2 and y^2 respectively. For visualisation, the ellipse is plotted by using the parametric variable $\chi \in [0°,360°]$:

$$\begin{pmatrix} x \\ y \end{pmatrix}_{\text{ellipse}} = \begin{pmatrix} \cos\vartheta & \sin\vartheta \\ -\sin\vartheta & \cos\vartheta \end{pmatrix} \cdot \begin{pmatrix} (1+e_x)\sin\chi \\ (1+e_y)\cos\chi \end{pmatrix}. \tag{3.7}$$

The angle χ is a parametric variable which does not refer to a physical surface. It should not be confused with the angles in stress ellipses or Mohr circles.

Other Strain Properties

Rotation
The angle by which a material line, that coincides with one of the principal strain axes, is rotated is given as

$$\tan\omega = \frac{c-b}{a+d} \tag{3.8}$$

(Ramsay & Huber, 1983). This angle is a measure for the amount of simple shear in the deformation. In the case of pure shear, $\omega = 0°$, while for simple shear $0 < |\omega| << 90°$, where the positive sign represents sinistral sense of shear. The definition of rotation is similar to that of the "vorticity number" W_k by Means et al. (1980), leading to comparable characteristics for the two properties.

Ellipticity
The ellipticity of the strain ellipse can be found by dividing the two principal stretches:

$$R = \frac{1+e_1}{1+e_2}. \tag{3.9}$$

Dilatation
The dilatation is the determinant of the strain matrix minus one, or

$$\Delta = |\hat{\varepsilon}| - 1 \tag{3.10}$$

(Ramsay & Huber, 1983). That is, the dilatation is the relative change of area. A dilatation of zero therefore corresponds to no change of area, dilatation of one means doubling of the area. Negative dilatations between minus one and zero correspond to a reduction of the area. Dilatations smaller than minus one indicate flipping of the triangle in question along one of its sides.

Strain Tensor
The strain matrix ε also relates to the displacement gradient matrix $\partial_{ui}/\partial_{xj}$ as

$$\begin{pmatrix} \partial u_1/\partial x_1 & \partial u_1/\partial x_2 \\ \partial u_2/\partial x_1 & \partial u_2/\partial x_2 \end{pmatrix} = \begin{pmatrix} a-1 & b \\ c & d-1 \end{pmatrix}, \tag{3.11}$$

and the strain tensor ε_{ij} is the symmetric part of the displacement gradient matrix

$$\varepsilon_{ij} = \begin{pmatrix} a-1 & (b+c)/2 \\ (b+c)/2 & d-1 \end{pmatrix} \tag{3.12}$$

(Ranalli, 1987).

The strain tensor can be split into its isotropic and deviatoric parts $\varepsilon_{ij} = \varepsilon_{isoij} + \varepsilon_{devij}$ (Etchecopar et al., 1981). The isotropic strain represents the volumetric dilatation and can be expressed as the mean of the diagonal elements:

$$\varepsilon_{\text{iso}ij} = \delta_{ij}\frac{1}{2}\sum_k \varepsilon_{kk} = \delta_{ij}\varepsilon_{\text{iso}}. \tag{3.13}$$

Note that in the case of small deformations (a - 1, d - 1, b, c << 1), $\varepsilon_{iso} = \Delta$.

Stress Analysis

Viscosity
As mentioned above, the temperature distribution in the model could be recovered from the infra-red data. For the materials used in these experiments the function $\eta(T)$ was known. Using the Arrhenius Equation 2.15 and the data given in Table 7 allow to calculate the viscosity η from the temperature T.

The basis for these temperature data were the infra-red images, each consisting of 300 x 200 pixels. The "window" of the experiment contained about 290 x 130 pixels. In practice, the calculation of the viscosity was made for each pixel. The viscosity was then averaged for the triangle used to determine the deformation (on average about 60 pixels per triangle). Together with the strain tensor, the viscosity allowed to calculate the stress within the model.

Stress
For Newtonian materials, the relationship between the strain rate tensor and the stress tensor is given by

$$\dot{\varepsilon}_{ij} = \eta\sigma_{ij}, \tag{3.14}$$

where the viscosity is scalar. Thus, the two tensors have the same mathematical properties, only the eigenvalues differ in the factor η.

	grain size	fraction	angle of rest	ϱ_{bulk}	ϱ_{grain}	porosity
Material	mm	%	°	kg m^{-3}		%
Jet-Plast	0.063 – 0.125	24	37.0	732	1820	60
Jet-Plast	0.125 – 0.200	41	37.3	740	1780	58
Jet-Plast	0.200 – ∞	10	36.0	708	2270	69
Sand	0.080 – 0.200		34.0	1565	2530	38
Coloured Sand	0.080 – 0.200		35.6	1569	2390	36
Jet-Plast mean	0.063 – 0.200		36.8	736	1800	59
Sand mean	0.080 – 0.200		34.8	1567	2460	37

Table 5. Properties of brittle materials used. The plastic powder was sieved before analysis, the remaining 25% had a grain size smaller than 0.063mm and were not used. The angle of internal friction was determined measuring the angle of rest of small piles of the material (±2°). The densities (±8 kg m-3 and the porosity (±2%) were obtained using standard techniques.

		v_{L}	v_{N}	h	η	T
Thrust	Wedge	µm/s	cm/a	cm	rel.	C
T1	W1	40	5.0	17.0	1	42
T2	W2	20	2.5	17.0	1	42
T3	W3	8	1.0	17.0	1	42

Table 6. Experiments described utilising wax. Three experiments were done using a simple megathrust geometry, three more incorporating a weak wedge instead of the thrust. Configuration, convergence velocity (laboratory and natural), initial model thickness, relative viscosity and the resulting mean temperature of the wax are given for each experiment (ID used in text). Experiments T1-T3 and W1-W3 allow to compare the effect of the convergence rate, experiments C1-C3 were performed to examine the influence of the absolute scaling. Experiment C1 is a repetition of experiment T2. C2 is a "small, quick and warm" experiment, representing the same scenario as C3, with the length scale reduced by 1.7.

The stress tensor links a surface normal *n* to the traction r_n acting on that surface via

$$\vec{r}_n = \sigma_{ij}\vec{n} \tag{3.15}$$

(Ranalli, 1987). A vector which, when transformed with a tensor, remains its direction and only changes its length is called an eigenvector to that tensor. The change of length is called the eigenvalue (Kowalsky, 1979, r≠ 0).

The eigenvectors of the strain tensor coincide with the principal axes of the strain ellipse and represent the principal strains (Ramsay & Huber, 1983). The eigenvectors of the stress tensor represent the principal stress directions, the eigenvalues σ_i represent the absolute values of the principal stresses where $\sigma_1 \geq \sigma_2 \geq \sigma_3$ by convention (Ranalli, 1987). The principal strain axes and the principal stress axes coincide in pure strain, a simple shear component leads to angles in the range ±45° between principal strain and stress axes.

Similar to the strain tensor, the stress tensor can be split into its isotropic and deviatoric parts. If the material is considered to be incompressible, only the deviatoric stress contributes to the strain, and the isotropic strain is zero. In the experiments presented here, melt could move within the model (cf. Barraud et al., 2000). Consequently, some triangles could gain or lose volume and the isotropic strain was non-zero so that absolute stresses could not be calculated. Nevertheless, addition of an isotropic component to a tensor does not alter its eigenvectors. The eigenvalues do change, but the difference between any two eigenvalues remains the same.

For visualisation, the differential stress $(\sigma_1 - \sigma_3)/2$ and the direction of σ_1 are given in the Appendix. Note that the term "differential stress" should not be confused with "deviatoric stress" (Engelder, 1994). The former denotes the scalar difference between maximum and minimum principal stress, whereas the latter is a tensor with the sum of its main diagonal elements being zero. Deviatoric stress and differential stress can only be equal under isotropic stress conditions.

PT t Paths

Under certain conditions, the pressure-temperature-time history ("*PTt* path") of a rock sample could be deduced (e. g. Thompson & England, 1984). It was also possible to obtain the *PTt* path for given material points in the analogue experiments presented here. Because of the problems concerning scaling of temperature, the temperature paths for the model material points are more qualitative than quantitative. Nevertheless, a rough temperature scale can be given.

To be able to choose arbitrary material points, movement has to be interpolated from the known deformation field. Firstly, the triangle containing the initial point *p* has to be found. The coordinates of *p* can be expressed in terms of the corners r_0, $r_0 + r_1$ and $r_0 + r_2$ of that triangle (see Figure 4) by solving

$$\vec{p} = \vec{r}_0 + \zeta_1\vec{r}_1 + \zeta_2\vec{r}_2 \tag{3.16}$$

for ζ_1 and ζ_2. This is possible if the triangle has non-zero area.

Since the deformation is assumed to be homogeneous within the triangle, the "coordinates" (ζ_1, ζ_2) of *p* are constant during deformation.

The temperature of the material point can easily be inferred from the position and the temperature distribution. For the pressure, only the lithostatic pressure was given. Omission of "tectonic" differential stresses is also usual

	H	η_0
Material	kJ/mol	Pa s
Paraffin P57	406	8.44×10^{4}
Paraffin P53	415	2.45×10^{4}
Paraffin P43	437	1.11×10^{3}
Vaseline	76	4.09×10^{-2}
Colophony	313	5.65×10^{8}

Table 7. Properties of ductile materials used: Activation energy H and the viscosity •0 at the reference temperature 50ºC. These parameters allow the viscosity to be obtained from the temperature using equation 2.15. The values for P53 are based on interpolation.

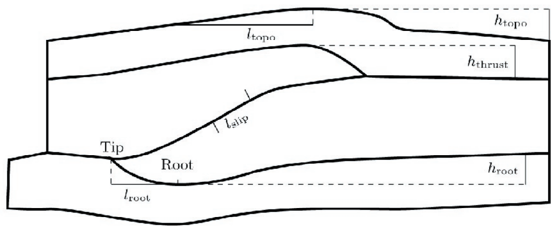

Figure 5. Description of geometrical measurements. The lengths indicated were measured for the six experiments presented, and compared in Figure 6.

in petrological studies, where pressure from *PTt* paths is converted to depth (e. g. Jamieson & Beaumont, 1988). Nevertheless, tectonic stresses might exceed the lithostatic pressure under certain conditions (Mancktelow, 1995).

The load of material above p is calculated by finding the material boundaries above it, and multiplication of the resulting heights with the respective densities following

$$P_{\mathrm{lith}} = \int_{\vec{p}_y}^{0} \varrho(y)\,\mathrm{d}y. \tag{3.17}$$

Implementation

The implementation of the analysis described above was achieved quite straightforwardly using the software “Mathematica” (Wolfram, 1991). Preliminary steps include digitisation of the marker positions at several time frames, triangulation and removal of triangles “outside” of the experimental domain.

Strain could be calculated incrementally during a time step, or as finite deformation relative to the initial state. The former was needed for later analysis of the stresses, the latter was advantageous for visualisation of the progressing deformation. Thus, starting from the coordinates of a triangle at two points in time, the following procedure was carried out:

1. Equation 3.4 solved for ε.
2. (x', y') rotated back to (x, y) by angle ϑ (equation 3.5) in the ellipse equation 3.6.
3. From the resulting equation, the coefficients of x^2 and y^2 were extracted to find the principal strains.
4. Strain ellipses plotted using equation 3.7.
5. Dilatation plotted using equation 3.10.
6. Rotation plotted using equation 3.8.
7. Ellipticity plotted using equation 3.9.
8. Viscosity averaged over each triangle.
9. ε_{ij} calculated from ε using equation 3.12.
10. σ_{ij} calculated from ε_{ij} using equation 3.14.
11. Eigenvectors of σ_{ij} calculated.
12. Differential stress calculated fromσ_{ij}.
13. Differential stress plotted.
14. Direction of the principal stresses (eigenvectors of σ_{ij}) plotted.

All these steps should be taken literally. With “Mathematica”, modification of an equation by a coordinate transformation is as easily done as extraction of coefficients from the resulting equation or the calculation of eigenvectors of a tensor.

Results and Conclusions

Bulk Analysis

Geometry

To obtain information about the overall geometry, lengths have been measured at a comparable shortening of around 21%. The measured lengths according to Figure 5 are:

- l_{topo} the half width at half maximum of the topography,
- h_{topo} height of the topography,
- h_{root} vertical distance between root and uppermost interface between lower crust and upper mantle (root depth),
- l_{root} horizontal distance between tip of underthrusting slab and root (root width),
- h_{thrust} vertical distance between top of lower crust and lowermost interface between the upper and lower crust (overthrusting height),
- l_{slip} displacement along the thrust in the thrust experiments,

The measured lengths and some ratios thereof are presented in Figure 6. Since the two blocks of the “lower crust” deform internally, the above properties cannot be identified with common properties of thrusts such as “throw” and “heave” as defined by Twiss & Moores (1992).

In both the wedge and the thrust experiments, the wavelength of the topography increased with the convergence velocity. The height of the topography was more or less similar in all the thrust experiments, and increased with convergence rate in the wedge experiments. The overthrusting height behaved similarly. Therefore, all vertical movement along the thrust was transmitted to the surface. However, as no erosion or sedimentation was modelled, the height of the topography (up to 15 km) is grossly exaggerated in these experiments. The steepness of the topography htopo/ltopo in both cases did not vary much around 40%. The wedge experiments tended to have steeper topographies, steepness increasing with the convergence velocity.

The behaviour of the root could be correlated with the convergence velocity more easily in the wedge experiments than in the thrust experiments. In the former, the root depth decreased with increasing velocity. This trend was less clear in the thrust experiments. The root length in the wedge experiments increased with higher velocity, which could not be observed in the thrust experiments. Nevertheless, the root steepness hroot=lroot decreased

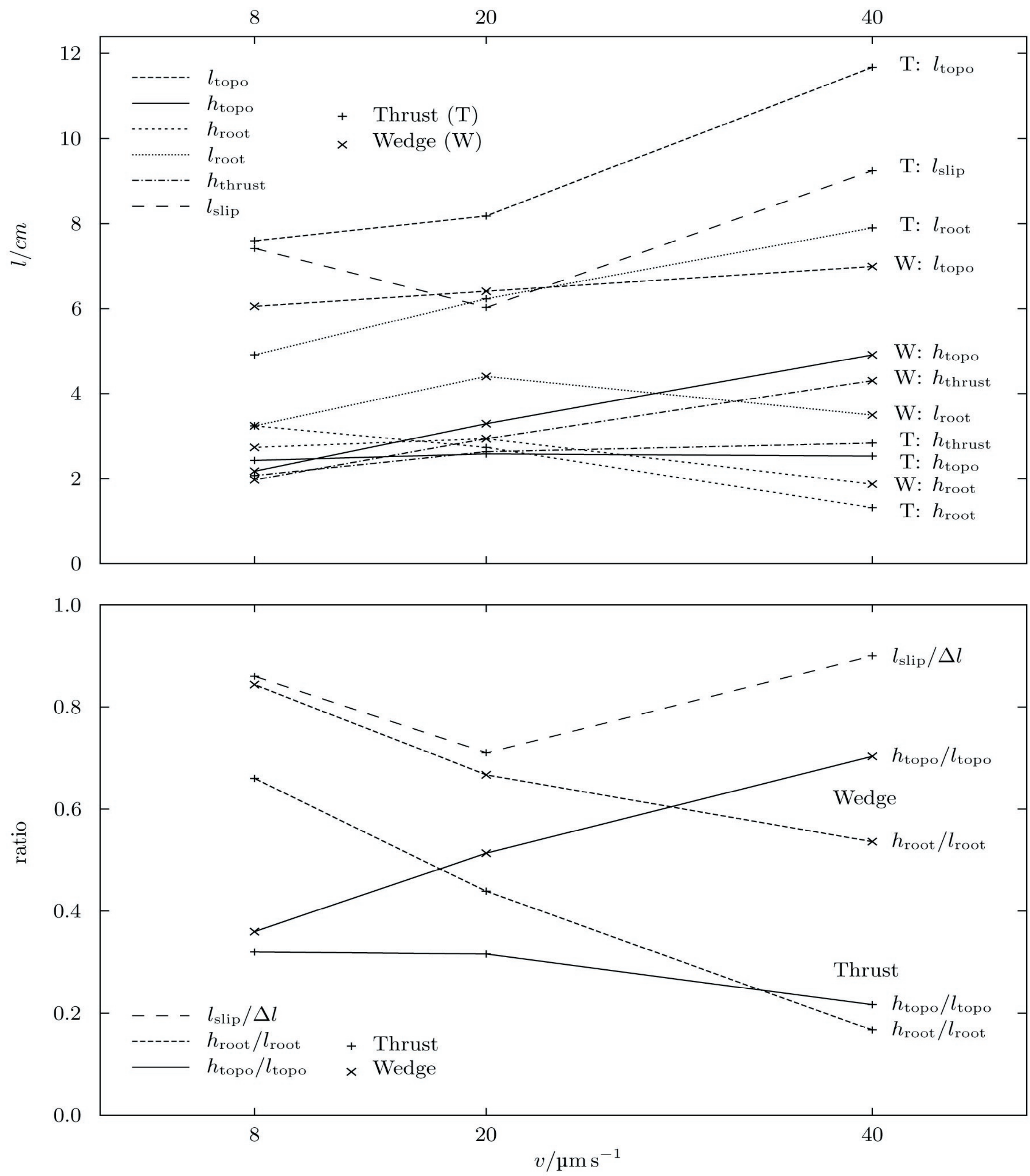

Figure 6. Lengths measured according to Figure 5, and some ratios thereof against convergence rate. Thrust and wedge experiments differ in the point style, corresponding lengths are assigned the same line style. The net slip only applies to the thrust experiments. In the lower plot, it has been normalized by the bulk shortening.

with increasing convergence rate in both experiment types, the trend being clearer in the wedge experiments.

The net slip shows no consistent behaviour towards the convergence velocity. Values between 6 and 9 cm correspond to 70-85% of the bulk shortening. As the thrust steepened from the initial 20° to 25° consistently in all thrust experiments, heave and throw are 90% and 42% of the net slip in these experiments.

Temperatures

The bulk temperatures measured in the experiments provide concise information about the stability of the overall temperatures (Figure 7). The preheat phase ensures a reasonably stable temperature field. Usually, 20 hours are sufficient for the temperatures to reach an equilibrium. During the deformation phase, the temperatures at the moving sensors remained constant within 1°C.

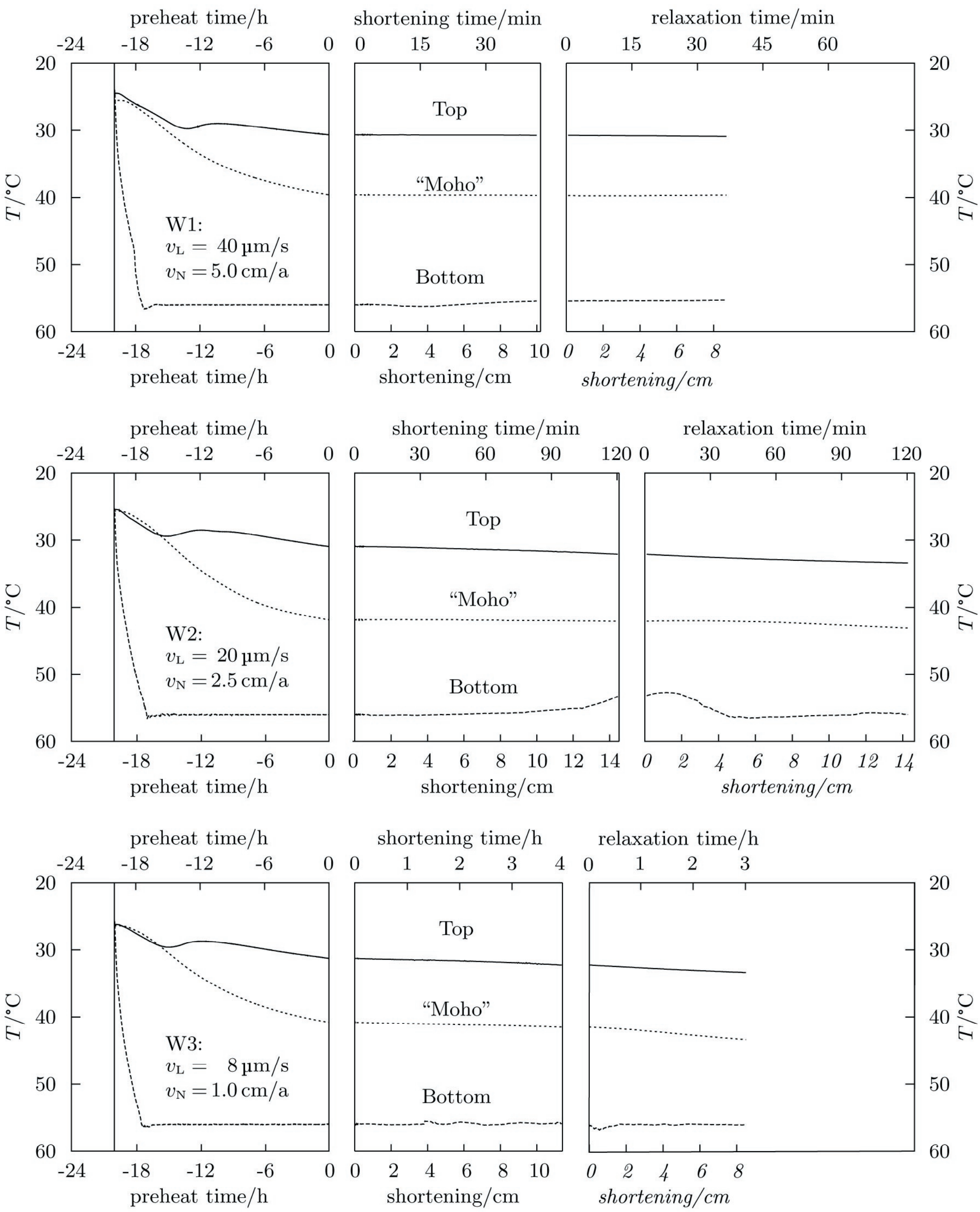

Figure 7. Temperature time series. The time series are split into the preheat, deformation and relaxation phases. In each graph, the temperature increases downwards, as in the model. For the preheat phase, the time scale was 24 hours. For the deformation phase, the temperature is plotted against shortening of the model. The length scale is identical for all plots. For the relaxation phase, time is converted to length using the deformation velocity. The "shortening" in the relaxation phase is indicated by italics. In fact, the model remains its length.

The temperature at the base of the model in some experiments fell by up to 5°C towards the end of the deformation. This is due to the "cold" tip of the footwall block being pushed downwards towards the stationary base sensor, displacing the "upper mantle". During the relaxation phase, the heating unit counterbalanced this disequilibrium within about 30 minutes.

Stresses

At the very start of each experiment, a pronounced peak in the bulk stress can be observed (Figure 8) during the first few minutes of the deformation. This peak was present in all experiments except T2. In that experiment, problems concerning the force transducer distorted the data. The rise time of these peaks was about twice their falling time,

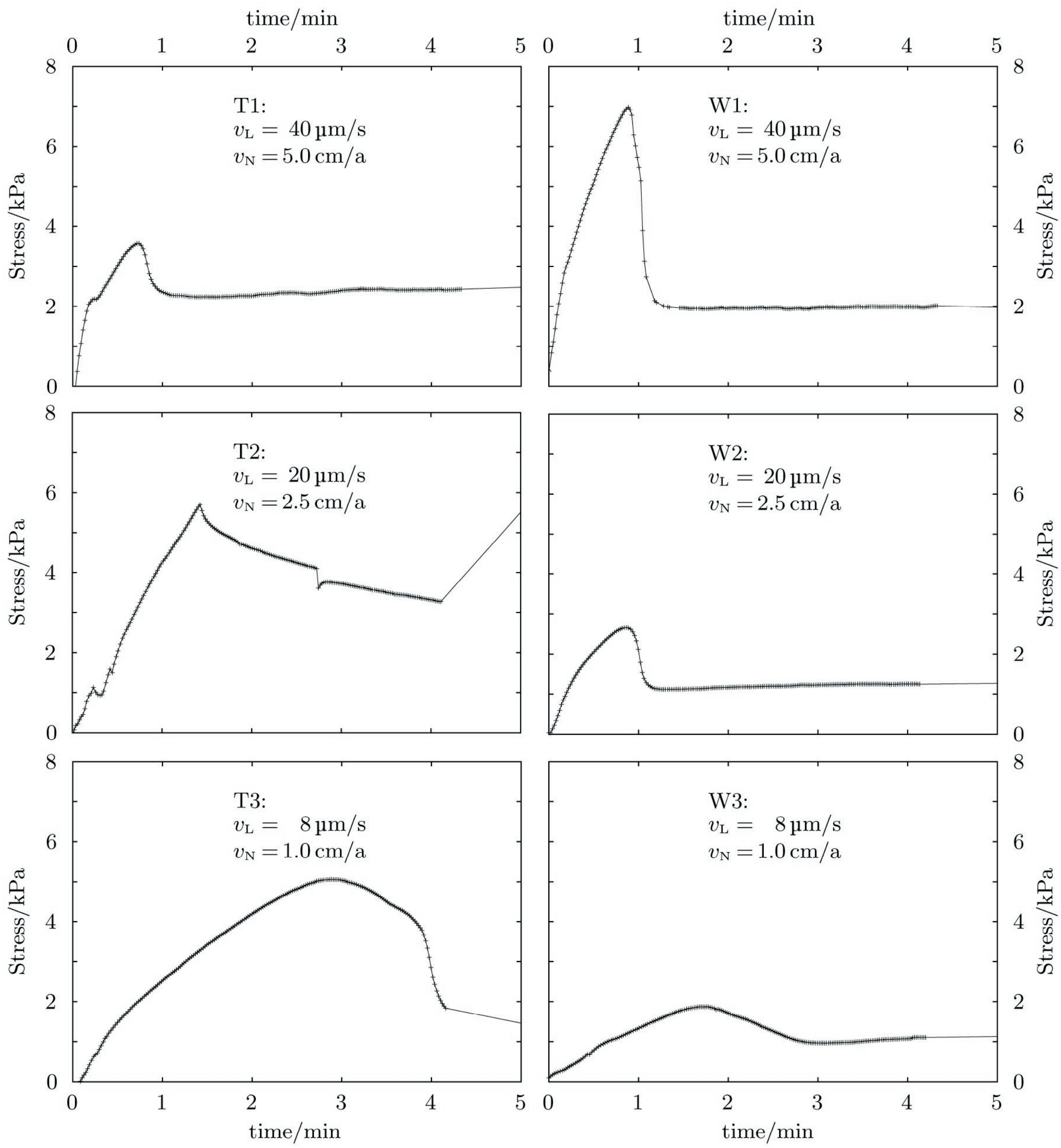

Figure 8. Initial stress peak recorded during the first few minutes of deformation. The peaks are due to initial sticking of the deformation plates. The data for experiment T2 also give evidence for a peak, although the data is distorted due to problems concerning the force transducer.

the height increasing with the convergence rate. This indicates a sticking phenomenon: Resistance must be overcome before steady-state deformation can occur.

After the initial sticking was overcome, the bulk stresses showed a further rise to about 1.8 kPa until about 4 cm (10 %) of shortening (Figure 9). The following decrease of the bulk stress is slowest or even non-existent in the fastest experiments. In these models, the isostatic equilibration was not as effective as in the other experiments. In experiment W1, no material flux underneath the pistons occurred. The slower experiments showed pronounced (T3 and W2) or even sharp (T2 and W3) decreases. Here, the weak material at the model base gave way quickly, reducing the apparent stress at the piston. Note that material behind the piston can lower the stress acting on the plate, even if the material level in the model does not change notably. Nevertheless, this correction (integration of the lithostatic pressure over the model height) would be less than 500 Pa, and variations after an initial phase of some minutes are small.

This process of rather sudden isostatic equilibration is an artefact of the experiments. The material flux under the pistons strongly depended on the temperature of the model base and therefore on the exact positioning of the lower temperature sensor. However, collapse processes have been predicted for orogenes by Dewey (1988), who even suggests the reversal of the overall stresses from horizontally compressive to extensive regimes

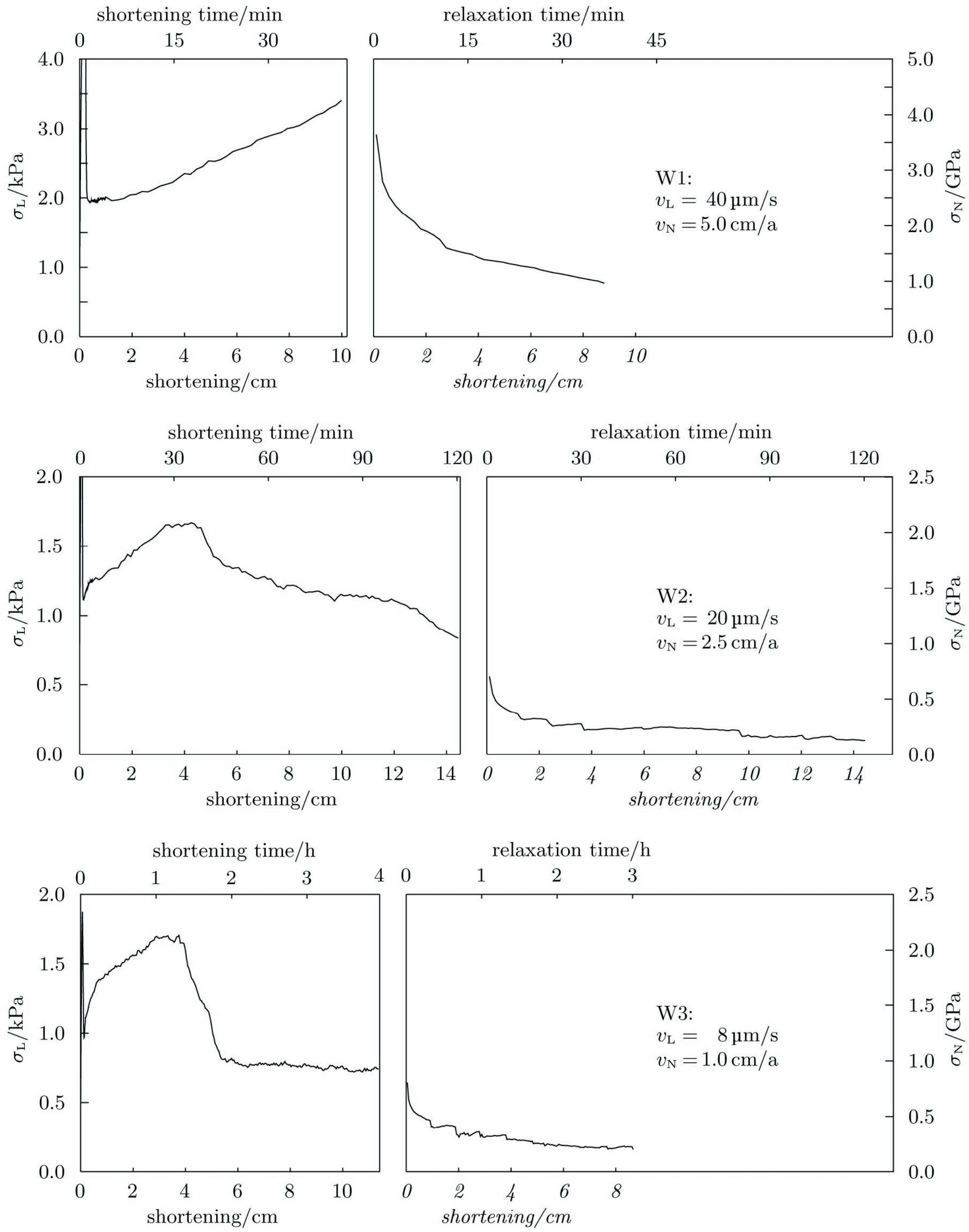

Figure 9. Bulk stress time series. Stress is plotted against the model shortening. For the relaxation phase, time is converted to length using the deformation velocity (cf. Figure 7). The stress scales are given for the laboratory and for nature. Note the different stress scale for the fast experiment.

due to gravitative effects. The latter processes have not been modelled in the experiments presented here, the observation was finished with the end of a relaxation phase about as long as the deformation required.

During the relaxation, the bulk stress decreased almost exponentially. The characteristic time for the first decrease was around 100 s, the overall characteristic time was on the order of some 10 minutes. In all experiments, a residual stress of ca. 100 Pa remained. This should not occur in a Newtonian material, and indicates that the waxes used in the experiments show non-Newtonian behaviour. A stress exponent larger than one would result in such a “threshold-stress”.

During the relaxation, the stress occasionally fell in “steps”. After abrupt decreases, the stress level remained constant for some minutes, or even rose again before the next decrease. This indicates some sort of “stick-slip” movement, and is probably due to the isostatic equilibration.

The molten material leaving the model domain underneath the pistons did not move continuously, but rather sporadically.

Detailed Analysis

As described in Section 3, deformation analysis could be done for each of the available triangles. The figures of the results are supplied as Quicktime movies for the six experiments listed in Table 6.

Dilatation (Click to view movies)

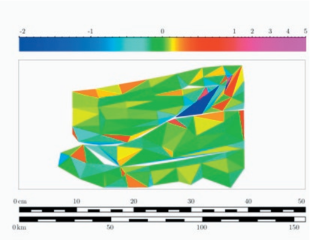

t1.dil.mov

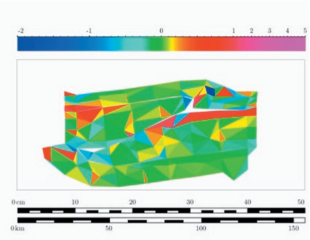

t2.dil.mov

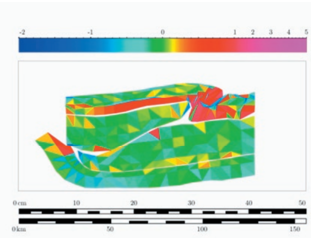

t3.dil.mov

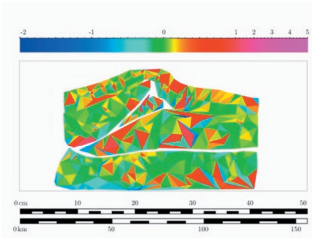

w1.dil.mov

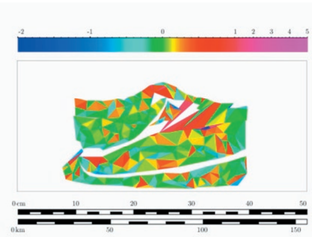

w2.dil.mov

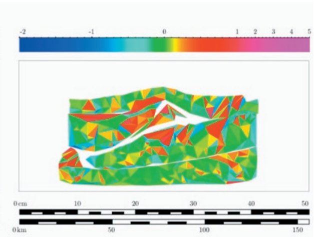

w3.dil.mov

The distribution of the dilatation shows a patchwork-like chaotic pattern. In all experiments, no more than about 2% of the triangles flip ($\Delta<-1$) at most 5% have dilatations smaller than -0.6. Large positive dilatations ($\Delta>2$) are similarly rare.

If large dilatations occurred in two adjacent triangles with opposite signs, this was probably an artefact of digitizing: If a marker position is digitized incorrectly, the areas of adjacent triangles change. Large dilatations were measured in the brittle part of the model, where the contrast of differently-coloured materials was used as markers. This contrast decreased during deformation, inhibiting accurate digitizing.

The large negative dilatations ($-1<\Delta<0$, blueish colours) occurred at the base of the upper mantle (e. g. Figures [w1.dil.mov] or [t1.dil.mov]) or in the lower left part of the hanging wall block of the lower crust (all experiments). These were areas where partial melting could be observed.

The analogue model presented here was not designed to incorporate partial melting. The effects showing dilatation (regardless whether due to movement of melt or due to digitisation errors) pose limitations for the data analysis. Nevertheless, neither the differential stresses nor the direction of the principal strain axes are influenced by the isotropic part of the stress (or, indeed the strain) tensor. The size of the strain ellipses as well as the ellipticity are altered by an isotropic part of the strain tensor and have to be used with care in the respective areas.

In experiments with a wedge, the wedge always contained triangles with rather large dilatations, probably resulting from movement of the material in the line of view (see e. g. [w1.dil.mov]).

Rotation (Click to view movies)

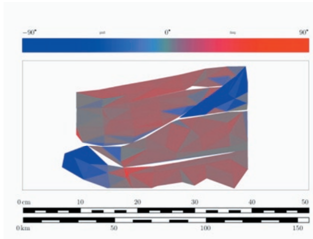

t1.rot.mov

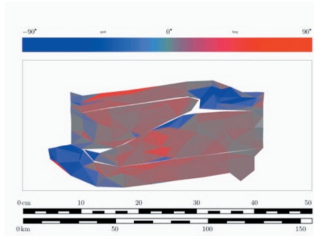

t2.rot.mov

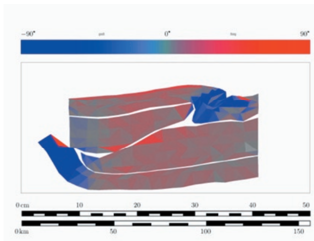

t3.rot.mov

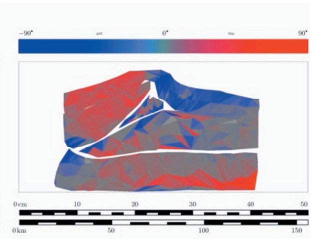

w1.rot.mov

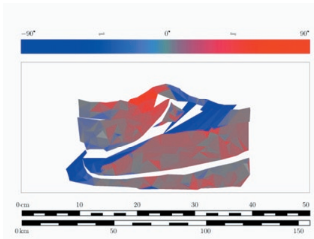

w2.rot.mov

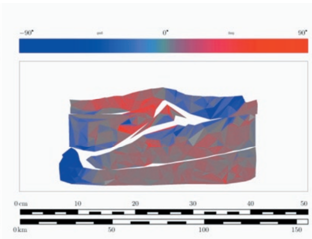

w3.rot.mov

All the experiments have some features of the rotational shear in common. Four areas show dextral shear (see e. g. [t3.rot.mov] or [w2.rot.mov]):

The left side of the upper mantle was rotated upwards because of the downward pushing slab of the lower crust.

The part of the brittle upper crust around the prolongation of the thrust/wedge showed strong clockwise rotation, caused by brittle material falling down the evolving slope.

The root of the footwall block of the lower crust was sheared by the compressive forces acting from the right while the movement of the tip was obstructed.

The left-hand side of the footwall block was rotated clockwise slightly.

Although the deformation along the thrust was dextral, the internal deformation in the two blocks of the lower crust adjacent to the thrust appears to be sinistral (e. g. [t2.rot.mov]). This was an effect of the rotation of the whole block, which was caused by steepening of the thrust.

Weak sinistral deformation in the right hand side of the upper mantle was a consequence of material flux underneath the right-hand piston out of the model domain (e. g. [w1.rot.mov]). It can be observed that the sinistral rotation in the hanging wall block of the lower crust was stronger in the experiments incorporating a weak wedge instead of a simple thrust (compare e. g. Figures [t1.rot.mov] and [w1.rot.mov]). This effect dominated in the fast experiments, and was weaker in the slow runs. In the wedge, both dextral and sinistral shear were present.

Ellipticity (Click to view movies)

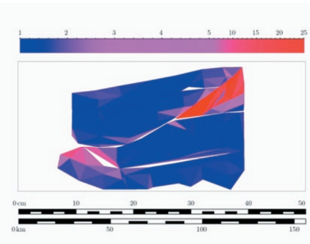

t1.elt.mov

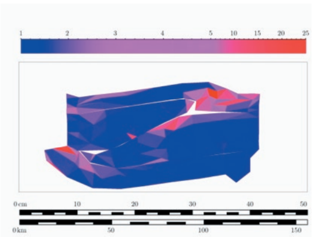

t2.elt.mov

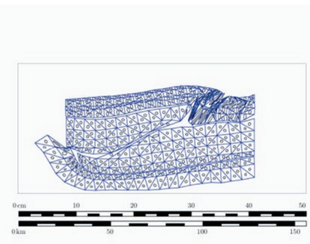

t3.elt.mov

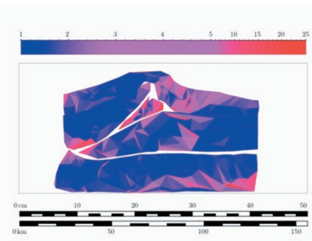

w1.elt.mov

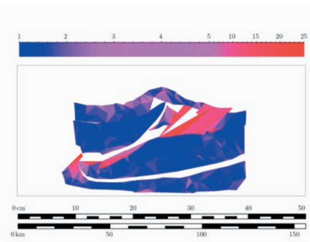

w2.elt.mov

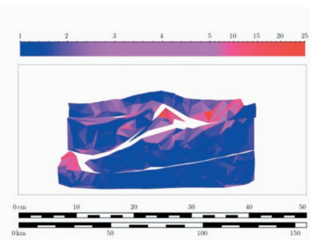

w3.elt.mov

To analyse the strain in the experiments, strain ellipticities were plotted. Together with the rotation data, the ellipticities allow to distinguish between pure shear and simple shear. Rotation in areas with low ellipticity is “rigid” body rotation, while $\omega \neq 0$ in domains of significant ellipticities indicates simple shear. Ellipticities larger than one in the absence of rotation are a result of pure shear. This way of distinction between simple shear and pure shear is complementary to the one given by Passchier & Trouw (1996).

It should be noted that large ellipticities coincide with negative rotations (dextral shear), as can be seen in Figures [w2.rot.mov] and [w2.elt.mov]. These areas were the only ones with large ellipticities. Obviously, pure shear only played a minor role in the deformation.

Furthermore, the positive rotations were caused by whole-body rotation rather than by a simple-shear component of the strain. Therefore, the correlation between the rotation in the hanging wall block and the convergence rate as mentioned in the previous section is due to the lower internal deformation in fast experiments. The gravitative stresses are weaker than the viscous stresses in this case.

Stresses

For the analysis of the stresses, both the direction of the maximum principal stress axis $\sigma 1$ and the differential stress $(\sigma_1\text{-}\sigma_2)/2$ are given. Whereas the directions do not depend on the viscosity of the materials, the differential stresses do. Therefore the latter are only given in the ductile materials.

Differential Stress (Click to view movies)

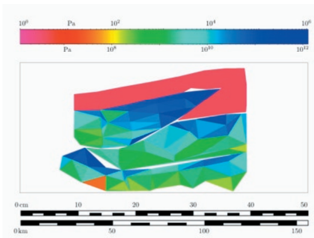

t1.dif.mov

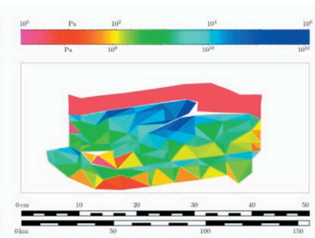

t2.dif.mov

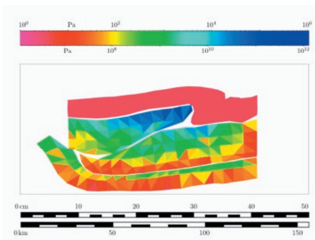

t3.dif.mov

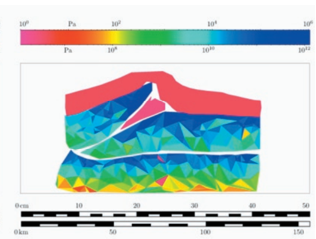

w1.dif.mov

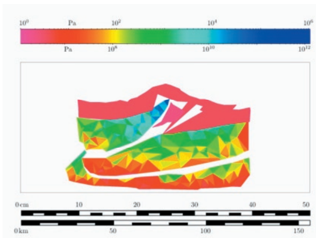

w2.dif.mov

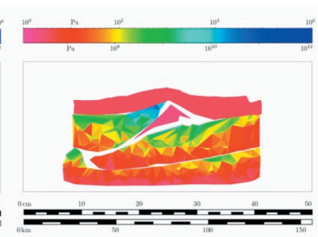

w3.dif.mov

The differential stress partly coincided with the temperature distributions. They were high in the upper parts of the two wax layers, and several orders of magnitude less in the lower parts. This is due to the temperature dependent rheology of the paraffin waxes: at higher temperature the viscosity is lower, and therefore at comparable strain rates lower differential stresses occur.

The stress distribution reflects the temperature field as well as the convergence velocity. The ductile materials were harder in lower temperature domains, and the overall stress was higher in the experiments with high convergence velocities. Higher bulk deformation rates lead to larger stresses if the viscosities (temperatures) are similar.

It could also be noted that after the deformation stopped, the stresses do not fall back to zero immediately, as was described in the bulk analysis and in Figure 9.

Again, this observation suggests that the material does not show exact Newtonian behaviour. In a linear viscous medium, stresses should decrease towards zero, while non-Newtonian materials can sustain stresses up to a certain threshold (σ_0 to reach a strain rate of ε_0 as in equation 2.8 for n>>1).

Direction of σ_1 (Click to view movies)

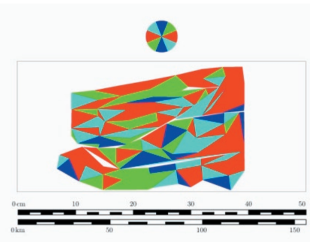

t1.sig.mov

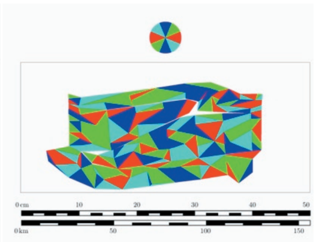

t2.sig.mov

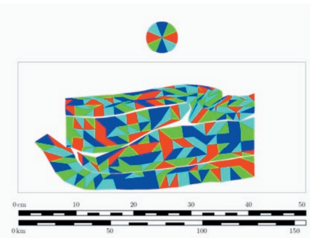

t3.sig.mov

w1.sig.mov

w2.sig.mov

w3.sig.mov

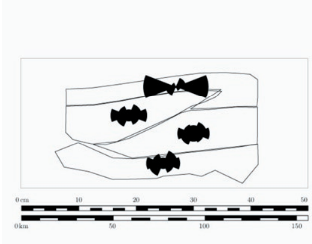

t1.ros.mov

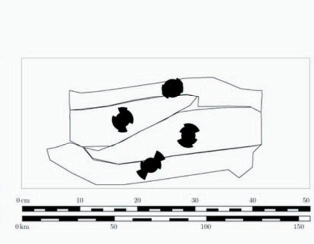

t2.ros.mov

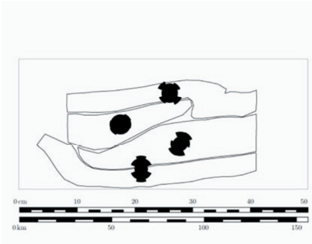

t3.ros.mov

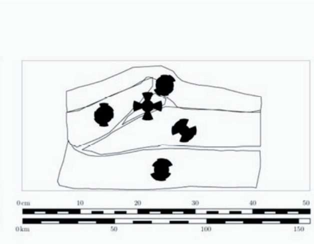

w1.ros.mov

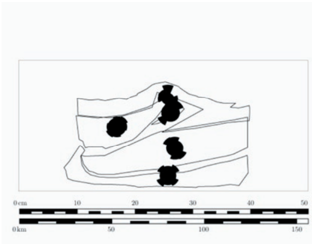

w2.ros.mov

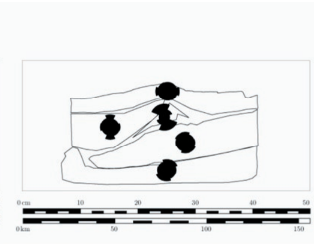

w3.ros.mov

The distribution of the direction of σ_1 in the upper crust shows a change from horizontal compressive stresses to vertical maximum stress or isotropic distribution. The distribution is not homogeneous: in the left part the direction points up-right, in the right half rather down-right (see e. g. [t2.sig.mov]).

In Figures [t1.sig.mov] and [w1.sig.mov] it can be seen that in the quick experiments, the directions in the hanging wall block of the lower crust change from being perpendicular to the thrust to a more or less isotropic distribution. Stress directions in the footwall block of the lower crust are rather isotropic, with a slight tendency to horizontal compressive regimes (e. g. [w3.dif.mov]). In the upper mantle the direction changes clearly from horizontal compression to horizontal extension (e. g. Figures [t2.dif.mov] or [w2.dif.mov]).

A common feature to all experiments is a flipping from compressive stresses in the upper mantle to extensive stresses at the end of the deformation. This reflects the “collapse” of the “orogen”, the mantle was pushed away to the sides to make place for the deepening root of the orogen. The overall process of collapse has been proposed by Dewey (1988). For the Tibet Region, England & Molnar (1997) calculated extensional stresses in regions of high topography, leading to horizontally compressive regimes at the flanks of the Himalayas.

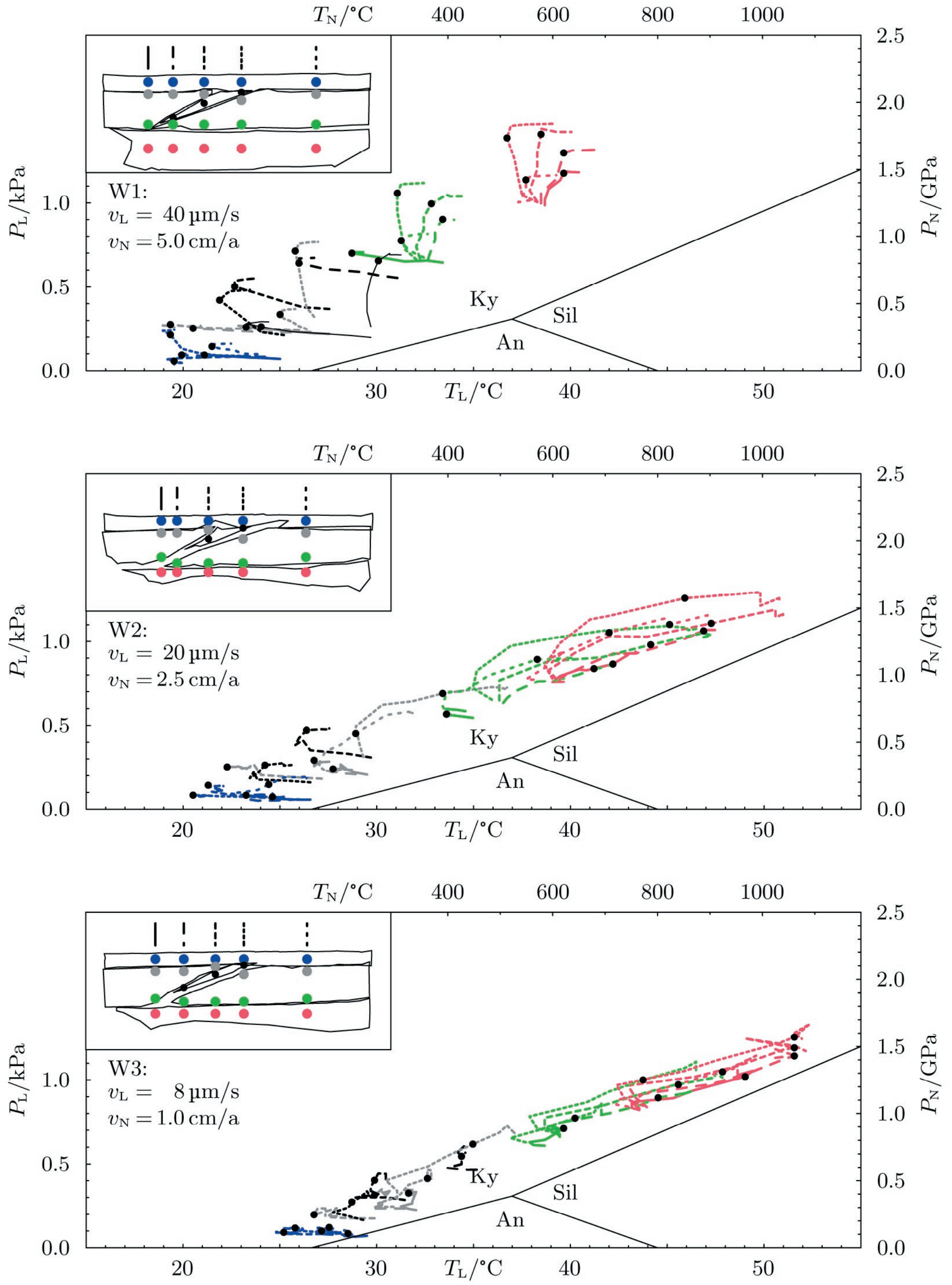

Figure 10. PTt paths in the experiments. The points selected for analysis are shown in the inserts. To assign a path to the initial location of the point, depth is coded as colour, the lateral position as line style. Paths originating in the same depth (same colour) start in the same PT domain. The end of the deformation phase is marked by a black dot. The paths for points of the wedge are coloured black. The phase diagram for aluminosilicates is given for raw orientation only. It is based on the "work-around" for scaling of temperature (equation 2.13), and not on phase transitions in the analogue material.

PT t Paths

In Figure 10 the *PTt* paths for some material points are shown. All paths are clockwise, i.e. an isothermal pressure increase is followed by a rise of temperature and pressure. The starting conditions of the paths correspond to their initial position in the model. The initial temperature and pressure rise got steeper with increasing initial depth. The pressure rose for points originating under the "foreland", due to accumulating load above. For the points originating in the upper crust, the ones originating in the "hinterland" show no pressure increase. The temperature change for these points was within 5°C. For the experiments including a relaxation phase, the ends of the paths showed an isobaric temperature rise towards the end.

The points originally in the upper crust of the hinterland start with an isobaric temperature decrease, followed only by an isobaric temperature increase in the relaxation phase. For the fast experiment including a wedge (W1), the

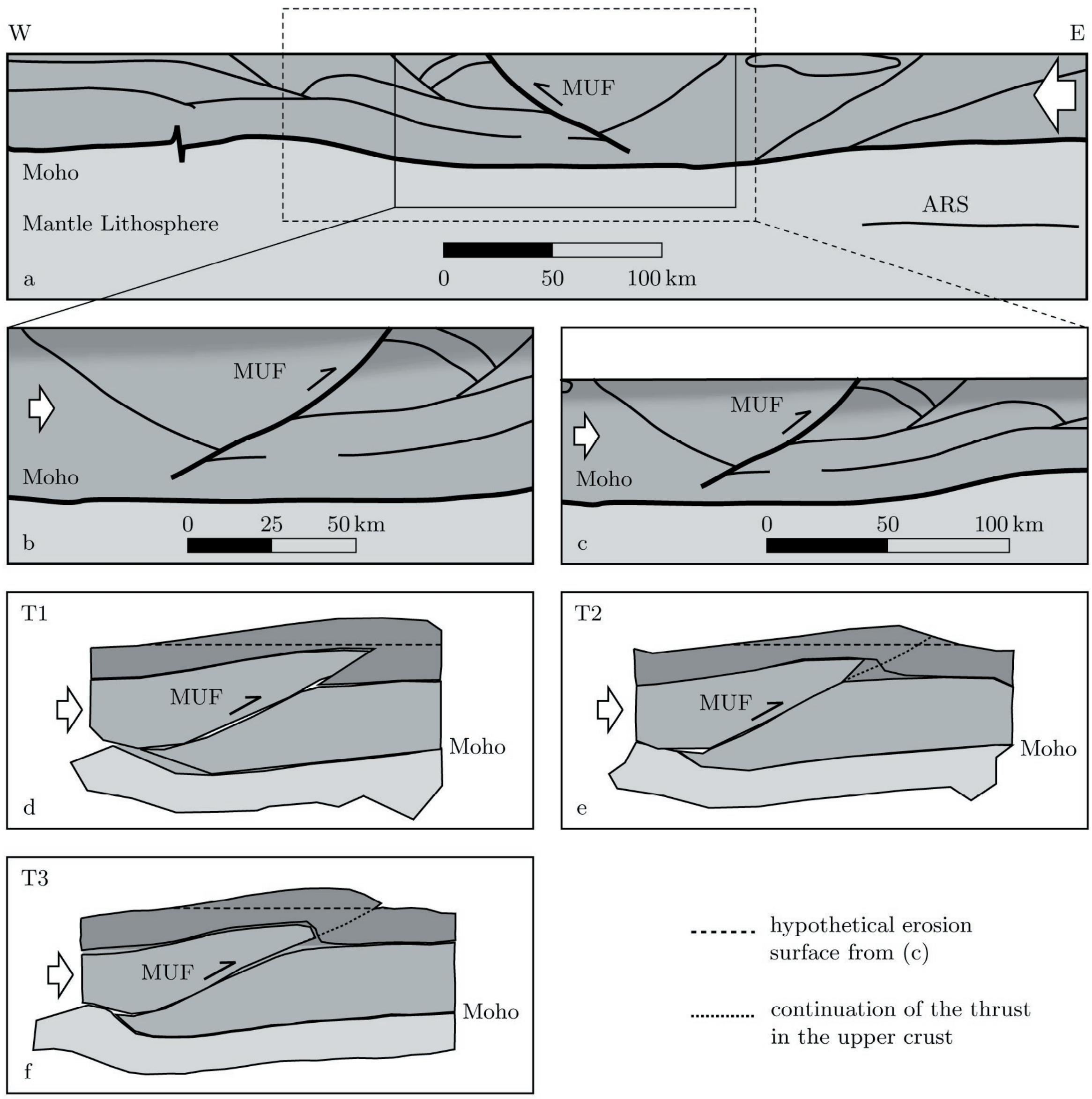

Figure 11. URSEIS Interpretation and correlation with analogue models. (a) Interpretation of "Urals Seismic Experiment and Integrated Studies", reproduced after Steer et al. (1998): The Main Uralian Fault (MUF) is the dominant feature, besides the Moho. Interpretation of the Alexandrovka Reflection Sequence (ARS) is still unclear. (b) Enlargement of inset in (a), according to the scaling of the experiments presented. East and West are reversed for coincidence with the analogue experiments. (c) Enlargement of the dashed inset in (a), corresponding to a length scaling about 30% smaller than in the experiments. (d) - (f) sketches of the experiments T1 - T3. The angle of the thrust corresponds well to the angle of the MUF. The thickness of the crust appears to be scaled correctly within 30 %. Topography of the real Moho is less than in the experiments, probably due to the longer equilibration.

uppermost points of the lower crust behaved similarly.

The clockwise form of the *PTt* paths has been described by England (1987) for diffuse continental deformation. The initial isobaric temperature decrease for the area described above has been predicted by England & Thompson (1984) and Thompson & England (1984) from numerical calculations for regions where the crust has been thickened by thrusting.

Natural rocks in orogenic scenarios are brought to the surface by erosion. Therefore, they show a geothermal decrease of temperature and pressure at the end of the PTt path. This end (a straight line to the "surface" conditions, 20°C, 0 GPa) must be added to paths shown in Figure 10.

Conclusions

Modelling

The outcome of the experiments lead to various implications. Even the first experiments using colophony demonstrated the ability of the apparatus to maintain a temperature gradient and to deform a layer of rheologically layered material. The reverse thrust scenario being compressed with a strain rate of $10^{-14}s^{-1}$ (scaled to nature) showed isotherms being advected by the moving material. In this case, the conductive thermal equilibration is slower than the advection. The deformation of isotherms has been performed and documented, and also in slower experiments it could be shown that the thermal equilibration did not keep up with the ongoing deformation.

The experiment using sand as brittle upper crust implies the necessity for correct scaling of density. A heavy orogen building up causes an instability, sinking down to the model base. In a natural scenario, the density inversion would lead to subsidence of the dense material, down into the mantle. However, such a scenario is extremely unrealistic. Nevertheless, the rise of diapirs could be modelled using this combination of materials.

During the relaxation phase of the experiments, the stresses in the upper mantle changed from a horizontally compressive to an extensional regime. This is in accordance with the predictions by Dewey (1988) or England & Thompson (1984), who, however, suggested time scales of up to 120Ma for the extension and erosion of the orogenes. The relaxation phase also suggests that the paraffin waxes used as analogue materials do not show completely Newtonian behaviour. This is in accordance with measurements of Mancktelow (1988).

Urals

Although the analogue experiments presented were done primarily to demonstrate the possibility of scaled thermomechanical modelling, they still can be compared to real geological scenarios. The models shown scale to around 150km in length and incorporate the crust and the lithospheric mantle (50km thickness). The pre-defined weak zones affect the lower crust, but quickly penetrate the upper crust. The mantle showed ductile deformation only. The shear zone of the lower crust did deform the Moho, but the mantle did not develop shear zones.

A scenario containing a large thrust can be found in the urals, at the boundary between Europe and Asia. The collision of the Eastern European and the Kazachian plate started around 310Ma ago in the Middle Carboniferous (Zonenshain et al., 1994). During the collision, the shortening along the Main Uralian Front (MUF) was between 12.5km and 16.7km (Perez-Estaun et al., 1997), and convergence rates between 1 cm/a and 3 cm/a can be assumed (Zonenshain et al., 1994). The interpretation of the “Urals Seismic Experiment and Integrated Studies” (URSEIS) profile given by Steer et al. (1998) shows various structures, the MUF and the Moho being the most prominent ones (Figure 11). According to Steer et al. (1998), the Moho is a structural detachment, as is the case in the analogue experiments. The dip of the MUF corresponds well to the dip of the thrust in the analogue experiments presented, the scaling of length being correct within 30%. Since the Uralian Orogenesis ended about 210Ma ago (Echtler & Hetzel, 1997) and shows no significant remobilisation (Seward et al., 1997), the Urals had more time to equilibrate than the corresponding relaxation time of the models. Therefore, the topography of the Uralian Moho is less intensive than in the analogue model adjacent to the MUF.

The Alexandrovka Reflection Sequence (ARS) in the URSEIS profile at a depth of 80-100 km coincides with the base of the experiments. It can be interpreted as a continuation of the MUF, as a rheological boundary due to material or phase changes, or as a local fault zone within the mantle (Steer et al., 1998). The analogue experiments presented do not show evidence for penetration of the thrust zone into the mantle. If the ARS is a continuation of the MUF, it has not been formed synorogenically. Either the Alexandrovka Reflection Sequence is an older structure just as the MUF, or one of the alternative interpretations has to be used.

Himalayas

Sediments being subducted between colliding continents are probably softer than the continental plates (England & Holland, 1979). Due to buoyant forces, these sediments can be assumed to be extruded upwards during the collision (Mancktelow, 1995). This concept has been applied to the Higher Himalayan Crystalline (HHC) between the Main Central Thrust (MCT) and the Southern Tibetan Detachment (STD) (Grujic et al., 1996). The Himalayas are a comparatively young orogen: the MCT was active until 6-2 Ma ago (McDougall et al., 1993; Metcalfe, 1993). Therefore, the time scales for the collapse have not passed yet.

Although the length scales of the Higher Himalaya are larger than the lengths modelled by the analogue experiments presented, the geometry of the models is similar to that of the Himalayas according to the interpretation of the “International Deep Profiling of Tibet and the Himalaya” (INDEPTH) seismic profile (Figure 12). The convergence rate between the Indian and the Asian plates has been estimated by Henry et al. (1997) from various sources to be in the range 1.5-2.0 cm/a, which is in the range modelled by the analogue models presented. Since in the wedge experiments the deformation data obtained from the photos did not represent the deformation in the whole model, the data should be interpreted with care. Nevertheless, the wedge of weak material has been extruded between the two colliding blocks (Figure 13).

Newer numerical models of Beaumont et al. (2001) and analysis of topographical data by Clark & Royden (2000) show evidence for a channel of weak material instead of a wedge. To verify this concept by using analogue models, a way has to be found to model larger lengths either by choosing different materials, or by modifying the parameters of the apparatus.

The main points from the data analysis presented in the previous chapter apply to both types of orogenes. The steepness of the natural roots suggests convergence rates rather on the higher side of the ranges quoted above: 3 cm/a for the Urals, 2 cm/a for the Himalayas.

Dextral shear has been observed in the experiments at both ends of the thrust or the weak zone. The tip of the footwall block is not accessible in nature, but in the area of the upper crust where the thrust cuts the surface indicators for dextral simple shear should occur.

The analysis of the bulk stress data as well as the distribution of differential stresses predict remanent stresses in the orogenes, at least for some Ma after the deformation. In the Urals, these remanent stresses might have decayed by now, but in the Himalayas, remanent

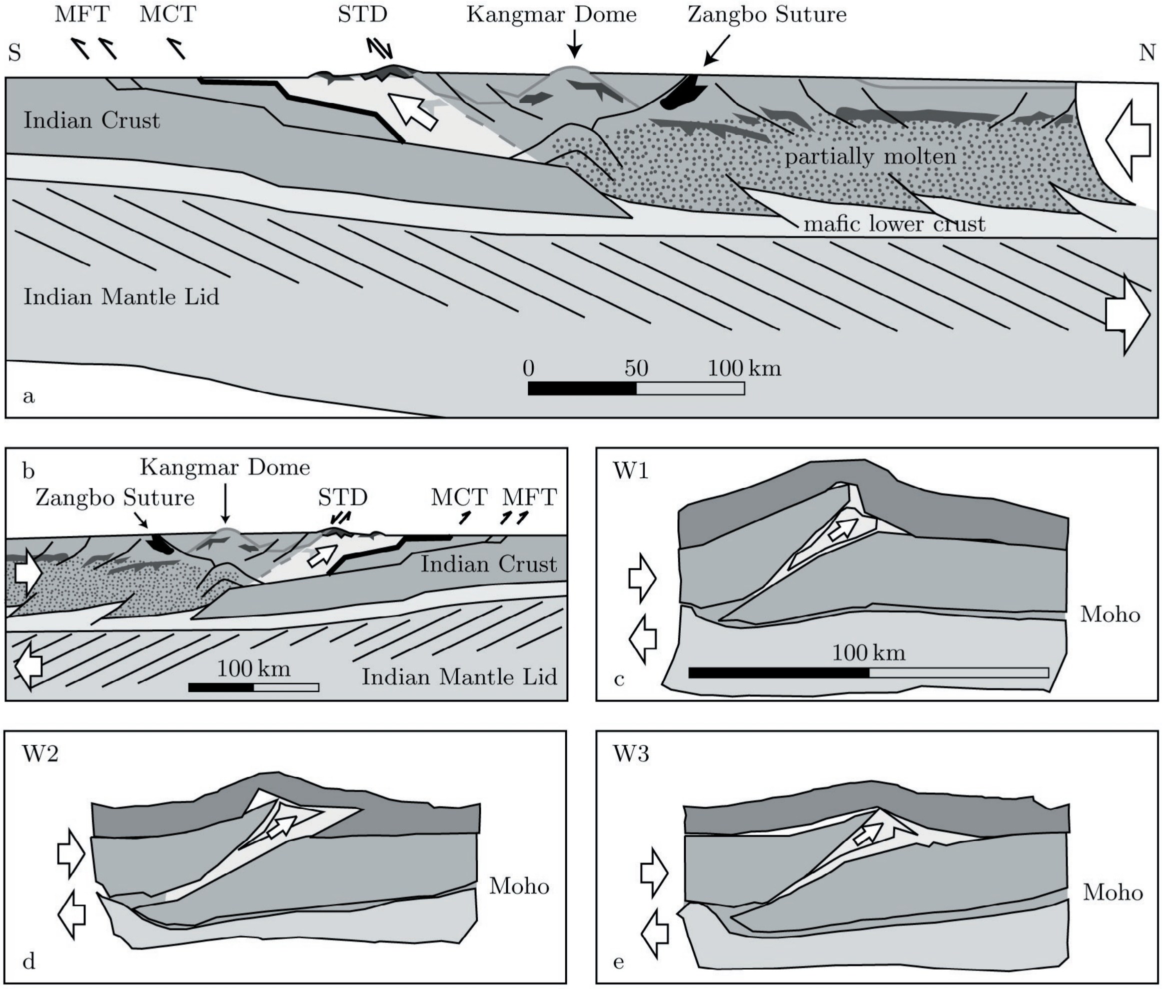

Figure 12. INDEPTH Interpretation and correlation with analogue models. (a) Interpretation of the "International Deep Profiling of Tibet and the Himalaya" seismic profile, reproduced after Nelson et al. (1996): The Main Frontal Thrust (MFT) and the Main Central Thrust (MCT) are reverse faults, the Southern Tibet Detachment (STD) is a normal thrust. In between MCT and STD, a wedge of material is thought to be extruded (Grujic et al., 1996). (b) Enlargement of the left part of (a), scaled to fit the analogue experiments presented. North and South are reversed for coincidence with the analogue experiments. (c) - (e) sketches of the experiments W1 - W3. The geometry of the wedge as well as the topography of the Moho (lower boundary of the mafic lower crust) coincide well. Nevertheless, the model represents a scenario 2.7 times smaller than the features of the Tibetan Himalayas.

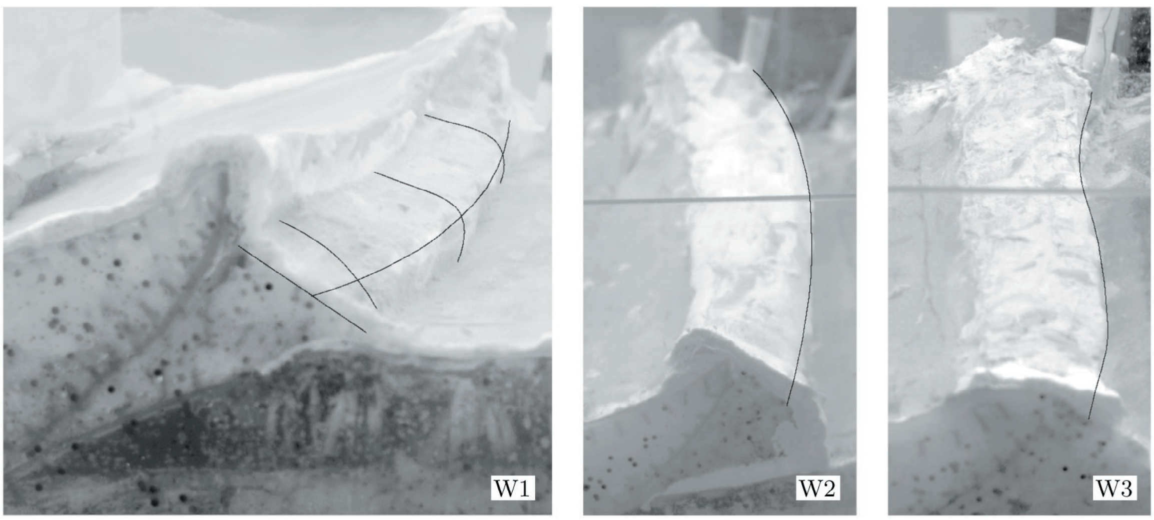

Figure 13. Photos of extruded wedges. The photos show details of the experiments containing a weak wedge. All experiments show extrusion of the wedge visible after removal of the Jet-Plast. For the wedge, the deformation seen at the model side is not representative for the whole experiment.

stresses are suggested by the analogue models.

The method of thermomechanical analogue modelling has proven the ability to produce, analyse and present data for continental collision on lithospheric scales. It has been shown that the set-up used is able to reproduce and visualize the deformation of isotherms. The machine is ready to use and the experimental techniques as well as the procedures for data analysis were tested and proved to give reproducable results.

Outlook

From the work with the apparatus for thermomechanical analogue modelling and from the first experiments, several suggestions arise for future machines and applications.

One important point is to learn more about the materials involved. For the analogue materials, measurement of the stress exponent n is necessary, as well more accurate estimates of the other flow properties. On the other hand, the data for natural rocks also lacks certain points. The data quoted in the literature is gained mostly from samples of some cubic centimetres, while it is applied to layers some ten kilometres thick and at strain rates some orders of magnitude less than those used to obtain the data.

Maybe in future experiments it might also be possible to introduce the important surface process erosion and sedimentation, without disturbance of the thermal equilibrium. The use of microwaves could be a way to include local heat production into the model.

Presently (December 2001), the apparatus is used for a Masters Thesis (Diplomarbeit of Philip Schiwek) to examine the onset of subduction at the (still) passive continental margin of Galicia. For these experiments, the scaling of density is extremely important, and the use of thin layers of lead powder embedded into the wax layers seems to be promising.

The machine presented is able to produce extensional regimes as well as compressive scenarios. The rise of diapirs or rifting processes can be modelled, maybe using sand as a brittle overburden. Additionally, the collisional experiments could be continued, examining the extensional phase of the collapse

In future thermomechanical experiments, the bottom temperature sensor should be fixed to the model base directly. All obstacles in the experimental domain must be avoided. The small floating PT100 temperature probes are permissible. Other sensors could be inserted into the models, such as piezoelectric stress sensors. Thus, the stress analysis presented in this work could be verified. Anyway, a second strain gauge for the second piston is necessary. Due to different material fluxes behind the pistons, the bulk stresses imposed to the plates are not equal. By also measuring the material level on the rear side of the pistons, the pure loading component could be identified.

A less steep temperature gradient in the model should be able to provide larger viscosity contrasts at the model Moho. Nevertheless, it is necessary to have the base of the model molten to decrease friction at the bottom of the model and to allow material flux behind the pistons for isostatic equilibration.

An important factor in the experiments is the analysis of the data obtained. As errors induced by the process of digitization of the marker positions can influence the results, an automated procedure for the strain analysis would largely improve both the quality and the quantity of data. It would also be easier to take into account more marker particles at more time steps.

For further experiments modelling the Higher Himalayas, the scaling of the experiments must be recalculated. Using a different set of gears, the motor could provide higher deformation rates, resulting in a smaller scaling factor for length, so that larger natural scenarios could be modelled. However, the experimental techniques for these models must also be refined to reduce boundary effects within the weak wedge or the newly suggested channel.

Probably one of the most important applications for thermomechanical analogue modelling lies in its interplay with numerical models. Although simulating large internal deformations in combination with discrete detachment zones still seems to pose numerical problems, the increasing power of computers keeps up with the refinement of data analysis in analogue experiments. The disadvantage of laboratory models to be limited to physical material properties does not exist in numerical models. On the other hand, analogue models include the physics implicitly, whereas numerical models can only simulate the processes they are programmed to simulate. Therefore, analogue models could be used to calibrate numerical models, which can then extend the results to nature. Only if a numerical model is able to reproduce a simple analogue model close enough, the computer code is justified to model geological scenarios.

Analogue modelling needs to be advanced further and further to provide an additional instrument for the Geologist. In this work, a major step forward has been done.

Acknowledgements

I want to express my gratitude towards Djordje Grujic, David Tanner and Jan Behrmann, who contibuted to this paper with many discussions. Beate Söhngen did the invaluable work of digitizing the data. Grant BE1041 by the Deutsche Forschungsgemeinschaft financed large parts of the project.

References

Barraud, J., Gardien, V., Allemand, P. & Grandjean, P. (2000): Analog modelling of the deformation of anisotropic partially molten rocks using paraffin wax. Geophysical Research Abstracts 2: SE24/p27.

Beaumont, C., Jamieson, R. A., Nguyen, M. H. & Lee, B. (2001): Himalayan tectonics explained by extrusion of a low-viscosity crustal channel coupled to focused surface denudation. Nature 414(6565): 738 - 742.

Bons, P. D., Jessell, M. W. & Passchier, C. W. (1993): The analysis of progressive deformation in rock analogues. Journal of Structural Geology 15(3-5): 403 - 411.

Brune, J. N. & Ellis, M. A. (1997): Structural features in a brittle-ductile wax model of continental extension. Nature 387(6628): 67 - 70.

Cadell, H. M. (1889): Experimental researches in mountain building. Transactions of the royal society Edinburgh 35: 337 - 357.

Carter, N. L. & Tsenn, M. C. (1987): Flow properties of continental lithosphere. Tectonophysics 136: 27 - 63.

Chemenda, A. I., Burg, J. P. & Mattauer, M. (2000): Evolutionary model of the Himalaya-Tibet system; geopoem based on new modelling, geological and geophysical data. Earth and Planetary Science Letters 174(3 - 4): 397-409.

Chemenda, A. I., Mattauer, M., Malavieille, J. & Bokun, A. N. (1995): A mechanism for syn-collisional rock exhumation and associated normal faulting: results from physical modelling. Earth and Planetary Science Letters 132: 225-232.

Clark, M. K. & Royden, L. H. (2000): Topographic ooze; building the eastern margin of Tibet by lower crustal flow. Geology 28(8): 703 - 706.

Cobbold, P. R. & Jackson, M. P. A. (1992): Gum rosin (colophony): a suitable material for thermomechanical modelling of the lithosphere. Tectonophysics 210: 255 - 271.

Cobbold, P. R., Rossello, E. & Vendeville, B. (1989): Some experiments on interacting sedimentation and deformation above salt horizons. Bulletin de la Societe Geologique de France 8: 453 - 460.

Davy, P. & Cobbold, P. R. (1991): Experiments on shortening of a 4-layer model of the continental lithosphere. Tectonophysics 188: 1 - 25.

Decker, E. R., Heasler, H. P., Buelow, K. L., Baker, K. H. & Hallin, J. S. (1988): Significance of past and recent heat-flow and radioactivity studies in the Southern Rocky Mountains region. Geological Society of America Bulletin 100: 1851 - 1885.

Dewey, J. F. (1988): Extensional collapse of orogenes. Tectonics 7(6): 1123 - 1139.

Ding, Z. (1984): Some formulae for calculating parameters of the strain ellipse. Tectonophysics 110: 167 - 175.

Echtler, H. P. & Hetzel, R. (1997): Main Uralian thrust and main Uralian normal fault; nonextensional Palaeozoic high-P rock exhumation, oblique collision, and normal faulting in the Southern Urals. Tera Nova 9(4): 158 - 162.

Engelder, T. (1994): Deviatoric stressitis; a virus infecting the earth science community. EOS, Transactions 75(18): 209 - 210.

England, P. C. (1987): Diffuse continental deformation; length scales, rates and metamorphic evolution. Philosophical Transactions of the Royal Society of London, Series A: Mathematical and Physical Sciences 321(1557): 3 - 22.

England, P. C. & Holland, T. J. B. (1979): Archimedes and the Tauern eclogites; the role of buoyancy in the preservation of exotic eclogite blocks. Earth and Planetary Science Letters 44(2): 287 - 294.

England, P. C. & Molnar, P. (1997): Active deformation of Asia: from kinematics to dynamics. Science 278(5338): 647 - 650.

England, P. C. & Thompson, A. B. (1984): Pressure-temperature-time paths of regional metamorphism; I, Heat transfer during the evolution of regions of thickened continental crust. Journal of Petrology 25(4): 894 - 928.

Etchecopar, A., Vasseur, G. & Daignieres, M. (1981): An inverse problem in microtectonics for the determination of stress tensors from fault striation analysis. Journal of Structural Geology 3(1): 51 - 65.

Fowler, C. M. R. (1990): The Solid Earth. Cambridge University Press, Cambridge, 472 pp.

Grujic, D., Casey, M., Davidson, C., Hollister, L. S., Kuendig, R., Pavlis, T. L. & Schmid, S. M. (1996): Ductile extrusion of the Higher Himalayan Crystalline in Bhutan; evidence from quartz microfabrics. Tectonophysics 260: 21 - 43.

Handy, M., Braun, J., Brown, M., Kukowski, N., Paterson, M. S., Schmid, S. M., Stockhert, B., Stuwe, K., Thompson, A. B. & Wosnitza, E. M. (2001): Rheology and geodynamic modelling: the next step forward. International Journal of Earth Sciences 90: 149 - 156.

Henry, P., Le Pichon, X. & Goffe, B. (1997): Kinematic, thermal and petrological model of the Himalayas: constraints related to metamorphism within the underthrust Indian crust and topographic elevation. Tectonophysics 273(1-2): 31 - 56.

Hoshino, K., Koide, H., Inami, K., Iwamura, S. & Mitsui, S. (1972): Mechanical properties of Japanese Tertiary sedimentary rocks under high confining pressures. Geological Survey of Japan Report 244.

Hubbert, M. K. (1937): Theory of scale models as applied to the study of geologic structures. Geological Society of America Bulletin 48: 1459 - 1520.

Hubbert, M. K. & Rubey, W. W. (1959): Mechanics of fluid-filled porous solids and its application to overthrust faulting. Geological Society of America Bulletin 70(2): 115 - 166.

Jamieson, R. A. & Beaumont, C. (1988): Orogeny and metamorphism; a model for deformation and pressure-temperature-time paths with applications to the Central and Southern Appalachians. Tectonics 7: 417 - 445.

Jamieson, R. A., Beaumont, C., Hamilton, J. & Fullsack, P. (1996): Tectonic assembly of inverted metamorphic sequences. Geology 24(9): 839 - 854.

Kirby, S. H. & Kronenberg, A. K. (1987): Rheology of the lithosphere; selected topics. Reviews of Geophysics 25(6): 1219 - 1244.

Kowalsky, H.-J. (1979): Lineare Algebra. de Gruyter, Berlin, New York, 9 edition, 367 pp.

Koyi, H. A. (2001): Modeling the influence of sinking anhydrite blocks on salt diapirs targeted for hazardous waste disposal. Geology 29(5): 387 -390.

Koyi, H. A. & Skelton, A. (2001): Centrifuge modelling of the evolution of low-angle detachment faults from high-angle normal faults. Journal of Structural Geology 23(8): 1179 - 1185.

Lallemand, S. E., Schnuerle, P. & Malavieille, J. (1994): Coulomb theory applied to accretionary and nonaccretionary wedges: Possible causes for tectonic erosion and/or frontal accretion. Journal of Geophysical Research 99(B6): 12 033 - 12 055.

Mancktelow, N. S. (1988): The rheology of paraffin wax and its usefulness as an analogue for rocks. Bulletin of the Geological Institutions of the University of Uppsala N.S.14: 181 - 193.

Mancktelow, N. S. (1991): The analysis of progressive deformation from an inscribed grid. Journal of Structural Geology 13(7): 859 - 864.

Mancktelow, N. S. (1995): Nonlithostatic pressure during sediment subduction and the development and exhumation of high-pressure metamorphic rocks. Journal of Geophysical Research 100(B1): 571 - 583.

McDougall, J. W., Hussain, A. & Yeats, R. S. (1993): The Main Boundary Thrust and propagation of deformation into the foreland fold-and-thrust beld in northern Pakistan near the Indus River. In: Himalayan Tectonics, Treloar, P. J. & Searle, M. P., eds., volume 74 of Special Publications, pp. 581 - 588. Geological Society, London.

Means, W. D. (1990): Kinematics, stress, deformation and material behavior. Journal of Structural Geology 12(8): 953 - 971.

Means, W. D., Hobbs, B. E., Lister, G. S. & Williams, P. F. (1980): Vorticity and non- coaxiality in progressive deformations. Journal of Structural Geology 2(3): 371 - 378.

Metcalfe, R. P. (1993): Pressure, temperature and time constraints on metamorphism across the Main Central Thrust zone and High Himalayan Slab in the Garhwal Himalaya. In: Himalayan Tectonics, Treloar, P. J. & Searle, M. P., eds., volume 74 of Special Publications, pp. 485 - 509.Geological Society, London.

Nataf, H. C. & Richter, F. M. (1982): Convection experiments in fluids with highly temperature-dependent viscosity and the thermal evolution of the planets. Physics of the Earth and Planetary Interiors 29: 320 - 329.

Nelson, K. D., Zhao, W., Brown, L. D., Kuo, J. T., Che, J., Liu, X., Klemperer, S. L., Makovsky, Y., Meissner, R., Mechie, J., Kind, R., Wenzel, F., Ni, J. F., Nabelek, J., Chen, L., Tan, H., Wie, W., Jones, A. G., Booker, J. R., Unsworth, M. J., Kidd, W. S. F., Hauck, M. L., Alsdorf, D., Ross, A., Cogan, M. J., Wu, C., Sandvol, E. A. & Edwards, M. A. (1996): Partially molten middle crust beneath southern Tibet; synthesis of Project INDEPTH results. Science 274(5293): 1684 - 1688.

Oldenburg, D. W. & Brune, J. N. (1972): Ridge transform fault spreading pattern in freezing wax. Science 178(4058): 301 - 304.

Oldenburg, D. W. & Brune, J. N. (1975): An explanation for the orthogonality of ocean ridges and transform faults. Journal of Geophysical Research 80(17): 2575 - 2585.

Ord, A. & Hobbs, B. E. (1989): The strength of the continental crust, detachment zones and the development of plastic instabilities. Tectonophysics 158: 269 - 289.

Passchier, C. W. & Trouw, R. A. J. (1996): Microtectonics. Springer Verlag, Berlin, Heidelberg, New York, London, Paris, Tokyo, Hong Kong, 289 pp.

Perez-Estaun, A., Alvarez-Marron, J., Brown, D., Puchkov, V., Gorozhanina, Y. & Baryshev, V. (1997): Along-strike structural variations in the foreland thrust and fold belt of the southern Urals. Tectonophysics 276(1-4): 265 - 280.

Piffner, O. A. & Ramsay, J. G. (1982): Constraints on geological strain rates; arguments from finite strain states of naturally deformed rocks. Journal of Geophysical Research 87(B1): 311 - 321.

Ramberg, H. (1967): Gravity, Deformation and the Earth's Crust. Academic Press, London, New York, 214 pp.

Ramsay, J. G. & Huber, M. I. (1983): The techniques of modern structural geology. Volume 1: Strain analysis. Academic Press, London, New York, 307 pp.

Ranalli, G. (1987): Rheology of the Earth. Allen & Unwin, Boston, London, Sydney, Wellington, 366 pp.

Ranalli, G. (2001): Experimental tectonics: from Sir James Hall to the present. Journal of Geodynamics 32: 65 - 76.

Rossetti, F., Faccenna, C., Ranalli, G. & Storti, F. (2000): Convergence rate-dependent growth of experimental viscous orogenic wedges. Earth and Planetary Science Letters 178(3 - 4): 367 - 372.

Rossetti, F., Ranalli, G. & Faccenna, C. (1999): Rheological properties of paraffin as an analogue material for viscous crustal deformation. Journal of Structural Geology 21(4): 413 - 417.

Sans, M. & Koyi, H. A. (2001): Modeling the role of erosion in diapir development in contractional settings. In: Tectonic Modeling: A Volume in Honor of Hans Ramberg,

Koyi, H. A. & Mancktelow, N. S., eds., Geological Society of America Memoir 193, pp. 111 - 122. Geological Society of America, Boulder, Colorado.

Sedgewick, R. (1988): Algorithms. Addison Wesley, Reading, Mass., 657 pp.

Seward, D., Perez-Estaun, A. & Puchkov, V. (1997): Preliminaryfi ssion-track results from the southern Urals | Sterlitamak to Magnitogorsk. Tectonophysics 276(1-4): 281 - 290.

Shemenda, A. I. & Grocholsky, A. L. (1994): Physical modeling of slow sea floor spreading. Journal of Geophysical Research 99(B5): 9137 - 9153.

Steer, D. N., Knapp, J. H., Brown, L. D., Echtler, H. P., Brown, L. D. & Berzin, R. (1998): Deep structure of the continental lithosphere in an unextended orogen; an explosive-source seismic reflection profile in the Urals (Urals Seismic Experiment and Integrated Studies (URSEIS 1995)). Tectonics 17(2): 143 - 157.

Thompson, A. B. & England, P. C. (1984): Pressure-temperature-time paths of regional metamorphism; II, Their inference and interpretation using mineral assemblages in metamorphic rocks. Journal of Petrology 25(4): 929 - 955.

Twiss, R. J. & Moores, E. M. (1992): Structural Geology. Freeman, New York, 532 pp.

Vendeville, B. & Cobbold, P. R. (1988): How normal faulting and sedimentation interact to produce listric fault profiles and stratigraphic wedges. Journal of Structural Geology 10(7): 649 - 659.

Weijermars, R. & Schmeling, H. (1986): Scaling of Newtonian and non-Newtonian fluid dynamics without inertia for quantitative modelling of rock flow due to gravity (including the concept of rheological similarity). Physics of the Earth and Planetary Interiors 43: 316 - 330.

Willett, S., Beaumont, C. & Fullsack, P. (1993): Mechanical model for the tectonics of doubly vergent compressional orogens. Geology 21(4): 371 - 374.

Wolfram, S. (1991): The Mathematica Book. Cambridge University Press, Cambridge, 1403 pp.

Wosnitza, E. M., Grujic, D., Hofmann, R. & Behrmann, J. H. (2001): New apparatus for thermomechanical analogue modeling. In: TectonicModeling: A Volume in Honor of Hans Ramberg, Koyi, H. A. & Mancktelow, N. S., eds., Geological Society of America Memoir 193, pp. 245 - 251. Geological Society of America, Boulder, Colorado.

Zonenshain, L. P., Korienevsky, V. G., Kzamin, V. G., Pechersky, D. M., Khain, V. V. & Matveenkov, V. V. (1994): Plate tectonic model of the South Urals development. Tectonophysics 109(1/2): 95 - 135.